Journal of Computational Physics **164,** 165–203 (2000)
doi:10.1006/jcph.2000.6596, available online at http://www.idealibrary.com on IDEAL®

A High-Resolution Procedure for Euler and Navier–Stokes Computations on Unstructured Grids

P. Jawahar* and Hemant Kamath†

*Department of Aerospace Engineering, Indian Institute of Science, Bangalore 560 012, India; and †Seminar für Angewandte Mathematik, Swiss Federal Institute of Technology, CH-8092, Zürich, Switzerland
E-mail: jawahar@aero.iisc.ernet.in, kamath@aero.iisc.ernet.in

Received November 10, 1999; revised June 27, 2000

A finite-volume procedure, comprising a gradient-reconstruction technique and a multidimensional limiter, has been proposed for upwind algorithms on unstructured grids. The high-resolution strategy, with its inherent dependence on a wide computational stencil, does not suffer from a catastrophic loss of accuracy on a grid with poor connectivity as reported recently with many unstructured-grid limiting procedures. The continuously differentiable limiter is shown to be effective for strong discontinuities, even on a grid which is composed of highly distorted triangles, without adversely affecting convergence to steady state. Numerical experiments involving transient computations of two-dimensional scalar convection to steady-state solutions of Euler and Navier–Stokes equations demonstrate the capabilities of the new procedure. © 2000 Academic Press

Key Words: unstructured grids, upwind, Euler, Navier–Stokes.

1. INTRODUCTION

Significant developments in algorithms for Euler and Navier–Stokes equations on unstructured grids have occurred in recent years. The primary motivation behind these developments is the ease with which unstructured grids can be generated around complex geometries in a relatively short turn-around time compared to that of block-structured grids. Furthermore, the random data structure associated with unstructured grids facilitates local concentration of the grid in locations of interest such as the near-field region of any object. Typically, unstructured grids are composed of simplices which are triangles and tetrahedra, respectively, in two and three dimensions. Unstructured-grid flow solvers, based on finite-volume discretization of the governing equations with upwind schemes, are preferred because of their robustness and their inherent ability to accurately represent the physics associated with linear and nonlinear waves at least in the limiting case of one-dimensional flows. Various upwind schemes in cell-center as well as cell-vertex formulations have been employed for solving a variety of flow problems on unstructured grids. A recent review by Venkatakrishnan [1] provides a perspective on unstructured-grid techniques and a complementary overview of the current state of the art has been presented by Mavriplis [2]. Barth's [3] report is an illuminating source of more comprehensive information on different aspects of unstructured grids and finite-volume solvers.

Accuracy is the most important aspect of any flow solver since it has a direct influence on the number of computational cells required to resolve a flow field to a desired extent as economically as possible. The inadequacy of a first-order accurate scheme, which is based on a piecewise constant representation, necessitates higher order implementation involving a gradient-reconstruction procedure. A higher order scheme not only yields improved resolution in regions of smooth flow but also significantly reduces the smearing of discontinuities. Initial attempts at implementation of higher order upwind schemes on unstructured grids focussed on extensions [4–7] of the one-dimensional reconstruction procedure based on the MUSCL approach [8], which had proved to be quite effective for structured-grid computations. However, because of the highly multidimensional nature of unstructured grids these techniques were only partially successful and it has been reported [9], but without numerical evidence, that poor quality results could be obtained on highly distorted grids even for smooth solutions. Limitations of a one-dimensional reconstruction procedure have been demonstrated in [10] where isotropic and anisotropic two-dimensional grids were employed and the incompatibility of the latter, for the simulation of a unidimensional shock-tube problem, was clearly revealed by the strong dependency of the results on grid connectivity. The introduction of a multidimensional gradient-reconstruction procedure for Euler computations, employing both cell-center and cell-vertex formulations on unstructured grids, could be attributed to the pioneering developments due to Barth and Jespersen [9]. A majority of the subsequent developments on higher order accurate unstructured-grid computations reported in the literature have followed the multidimensional approach.

Since modern upwind algorithms for compressible flow are designed for capturing discontinuities accurately, higher order schemes often produce nonphysical oscillations which can be effectively suppressed by employing limiters. However, it is known that limiters can adversely affect the convergence of the solution to steady state, and continuously differentiable limiters such as that of van Albada *et al.* [11] are generally preferred [12] even for structured-grid computations. The multidimensional limiter, developed by Barth and Jespersen [9] for Euler computations on unstructured grids, has been shown to stall [13] convergence to steady state. Furthermore, attempts [13, 14] to improve the convergence characteristics of limiters for unstructured grids have not been completely successful in yielding oscillation-free steady-state solutions. A particularly vexatious limitation in the form of an adjustable constant [13], which leads to a loss of robustness owing to a lack of universality, has introduced a measure of uncertainty in the application of unstructured-grid flow solvers for large complex problems.

The present research has been motivated by the necessity to improve upon the multidimensional gradient-reconstruction procedure for unstructured grids. The high-resolution [15] procedure proposed is shown to yield accurate solutions on a grid with poor connectivity. A new multidimensional limiter has been devised and its effectiveness has been demonstrated for strong discontinuities without adversely affecting convergence even on a grid which is composed of highly distorted triangles. The limiter, which is endowed with the property of continuous differentiability, does not clip smooth extrema. The gradient-reconstruction procedure is also beneficial for viscous flow computations on unstructured grids, which are considered to be relatively expensive as compared to structured grids because of the penalty associated with the employment of different computational stencils for inviscid and viscous terms apart from the more complicated formulae resulting from the inherently multidimensional construction. A unified approach for higher order accurate Euler and Navier–Stokes equations as presented here is helpful in reducing computational costs quite significantly apart from producing accurate solutions.

The paper has been organized in the following format. The next section briefly presents the governing equations for the two-dimensional compressible viscous flow and the finite-volume formulation. Sections 3 and 4 deal with the higher order accurate techniques and limiters, respectively. The results for several test cases from two-dimensional scalar convection to Euler and Navier–Stokes equations are presented in Section 5. Conclusions can be found in Section 6.

2. GOVERNING EQUATIONS AND FINITE-VOLUME FORMULATION

The governing equations for two-dimensional viscous compressible flow in Cartesian coordinates can be expressed in nondimensional form [16] as

$$\frac{\partial U}{\partial t} + \frac{\partial (F - F_V)}{\partial x} + \frac{\partial (G - G_V)}{\partial y} = 0, \tag{1}$$

where

$$U = \begin{pmatrix} \rho \\ \rho u \\ \rho v \\ \rho E \end{pmatrix}, \quad F = \begin{pmatrix} \rho u \\ \rho u^2 + p \\ \rho u v \\ \rho u H \end{pmatrix}, \quad G = \begin{pmatrix} \rho v \\ \rho u v \\ \rho v^2 + p \\ \rho v H \end{pmatrix} \tag{2}$$

$$F_V = \frac{1}{\mathrm{Re}_L} \begin{pmatrix} 0 \\ \tau_{xx} \\ \tau_{xy} \\ u\tau_{xx} + v\tau_{xy} - q_x \end{pmatrix}, \quad G_V = \frac{1}{\mathrm{Re}_L} \begin{pmatrix} 0 \\ \tau_{xy} \\ \tau_{yy} \\ u\tau_{xy} + v\tau_{yy} - q_y \end{pmatrix} \tag{3}$$

with

$$\begin{gathered} \tau_{xx} = 2\mu\frac{\partial u}{\partial x} - \frac{2}{3}\mu\left(\frac{\partial u}{\partial x} + \frac{\partial v}{\partial y}\right), \quad \tau_{yy} = 2\mu\frac{\partial v}{\partial y} - \frac{2}{3}\mu\left(\frac{\partial u}{\partial x} + \frac{\partial v}{\partial y}\right), \\ \tau_{xy} = \mu\left(\frac{\partial u}{\partial y} + \frac{\partial v}{\partial x}\right) \end{gathered} \tag{4}$$

and

$$q_x = -\frac{\mu}{(\gamma - 1)M_\infty^2 \mathrm{Pr}} \frac{\partial T}{\partial x} \quad \text{and} \quad q_y = -\frac{\mu}{(\gamma - 1)M_\infty^2 \mathrm{Pr}} \frac{\partial T}{\partial y}. \tag{5}$$

The two-dimensional system of equations can be expressed in integral form as

$$\int\!\!\int_{\mathcal{A}} \frac{\partial U}{\partial t}\, dx\, dy + \int\!\!\int_{\mathcal{A}} \left[\frac{\partial (F - F_V)}{\partial x} + \frac{\partial (G - G_V)}{\partial y}\right] dx\, dy = 0, \tag{6}$$

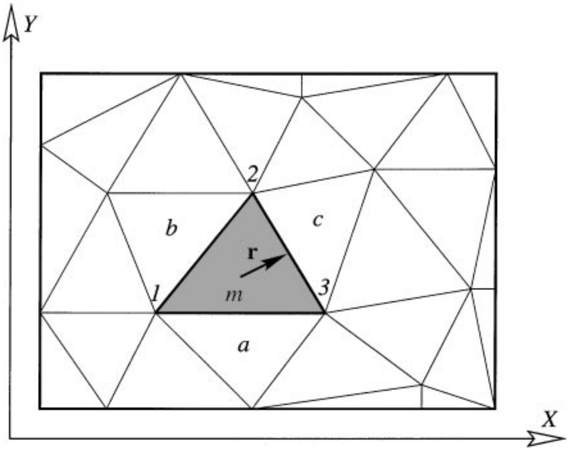

FIG. 1. Typical computational cell for an unstructured grid.

where $\mathcal{A}$ is the area of the computational cell, which is a triangle as shown in Fig. 1. The spatially integrated form of Eq. (6) can then be represented as

$$\mathcal{A}\frac{\partial U}{\partial t} + \sum_{l=1}^{3} [(F_N - F_{NV})\Delta s]_l = 0. \tag{7}$$

Here U is the cell-averaged value, F_N and F_{NV} are the inviscid and viscous flux vectors normal to an interface, respectively, and Δs is the length of an interface. The notations used here are the same as those in Ref. [16], which contains additional details in the context of structured grids.

The finite-volume approach is based on the physical concept of using macroscopic control volumes to numerically solve the governing equations (7). There are primarily two different ways of defining the control volume in the case of two-dimensional unstructured grids. The control volumes could be directly chosen as the triangles generated by the grid-generation process or alternatively either the median or centroidal dual to the triangles could be prescribed for this purpose. These definitions lead to cell-center and cell-vertex approaches, respectively, and there does not appear to be a consensus on which of the two is better with both being used extensively. In a centroidal dual the centroid of each of the triangles, which meet at a vertex, are directly joined to two of the immediate neighboring centroids. However, in a median dual the centroids are joined indirectly via the medians so that each dual edge comprises two line segments and then simplifications [10] are often introduced to reduce two flux evaluations for each edge to only one based on the normal vector to the edge corresponding to the centroidal dual. Such a simplification may not be justifiable for a pair of highly obtuse neighboring triangles where the line joining the two centroids may not even intersect the interface common to them [9]. Furthermore, it should be emphasized that computation of a flow field with a certain level of accuracy, achievable by satisfying the governing equations at a prescribed number of discrete locations, will require a coarser grid for a cell-center implementation as compared to a cell-vertex one. This is due to the number of triangles being double the number of vertices that define them in the case of an unstructured grid, whereas for a structured grid the cells, which are quadrilaterals, and the associated vertices are the same in number, neglecting boundary effects. Furthermore, the cell-center approach for a triangular unstructured grid can be regarded as a natural extension of its counterpart for a quadrilateral structured grid with its center at the centroid of the triangle and its three sides as interfaces as compared to four for the latter. In contrast to a cell-vertex method for an unstructured grid, the fixed number of interfaces associated with the cell-center method leads to a simpler implementation with an edge-based data structure and is well suited for the linear reconstruction procedure proposed in this paper. Also, it is one of the motivating factors in the design of the new multidimensional limiter.

The solution process begins by defining cell averages stored at the cell centers. Use of Riemann solvers to compute the numerical fluxes at an interface needs the prescription of a set of primitive variables on either side of an interface, known as “left” and “right” states. The edge-based data structure provides the necessary information to compute the interface numerical flux. For a first-order-accurate scheme the left and right states are nothing but the corresponding cell-center values. However, for second-order-accurate computations, information beyond the nearest neighbors is needed, where the constant distribution within a cell is replaced by a piecewise linear distribution. Second-order accuracy is achieved by a multidimensional linear reconstruction process which computes cell-centered gradients of the chosen set of primitive variables W. Referring to Fig. 1, we then obain the higher-order-accurate value W within a computational cell using Taylor’s series,

$$W = W_m + \nabla W_m \cdot \mathbf{r}, \tag{8}$$

where W_m is the cell-averaged value prescribed at the cell center, $\mathbf{r}$ is the vector extending from the cell center to the center of any of the three interfaces as shown, and ∇W_m is the cell-centered gradient, which is computed as described below.

Green’s theorem applied to a scalar relates the area integral of the gradient to its line integral over the boundary as

$$\int\!\!\int_A \nabla W \, dx \, dy = \oint_l W \mathbf{n} \, dl, \tag{9}$$

where $\mathbf{n}$ is the outward pointing local unit-normal vector and l denotes the boundary of A. If the gradient is assumed constant over the cell, the above equation yields

$$\nabla W_m = \frac{1}{A} \oint_l W \mathbf{n} \, dl. \tag{10}$$

Various second-order techniques, based on the multidimensional reconstruction procedure, differ in their estimate of this average gradient as determined by the closed path of integration l whose support is often called a stencil. A new gradient-reconstruction procedure, which is intrinsically endowed with a dependence on a wide stencil that serves to reduce the effects of grid sensitivity, is presented in the next section. The numerical flux can then be straightforwardly computed based on second-order left and right states. In the present investigation, the interface numerical flux is obtained using Osher’s flux-difference splitting scheme, which has been implemented as in Ref. [16] based on a grid-aligned locally one-dimensional construction for Euler and Navier–Stokes computations.

3. LINEAR RECONSTRUCTION

Details of various multidimensional reconstruction techniques are presented in this section. Existing methods, which are reported in the literature, are discussed in brief along with their advantages and shortcomings before the new reconstruction procedure is introduced. As mentioned earlier, several attempts have been made to extend the structured-grid techniques to unstructured grids; these have achieved only partial success owing to the pronounced grid sensitivity [9, 10] of the underlying one-dimensional reconstruction procedures. This indicates that the inherently multidimensional unstructured-grid geometry should be carefully taken into account when developing a higher-order-accurate reconstruction procedure. The proposed technique should possess dependence on a wide computational stencil to make it suitable for highly distorted triangles, which are often introduced by the grid-generation procedure even for a simple configuration. In contrast to a structured grid, where the number of quadrilaterals meeting at a vertex is precisely four, the number of such triangles is arbitrary in the case of an unstructured grid. Thus the reconstruction technique should not strongly depend on vertex values, which are obtained from the corresponding cell-centered values by some algebraic procedure, even though this would be desirable to an extent in a cell-centered formulation to naturally increase the width of the computational stencil.

To compare and contrast various reconstruction techniques a grid composed of equilateral triangles is chosen for illustration, but these procedures can be straightforwardly extended to more arbitrary triangulations. A multidimensional linear reconstruction technique for higher-order-accurate Euler equations on unstructured grids was first introduced by Barth and Jespersen [9]. They applied the Green–Gauss theorem to compute the gradient within a cell using the cell-center values of its neighbors. For the gradient computations, two different stencils were used as shown in Fig. 2. The first one is obtained by simply joining the centroids of the immediate neighbors (shown in Fig. 2 as dotted lines joining *abc*), but it may degenerate [9] into a straight line for highly distorted triangles. The second stencil (dashed lines in Fig. 2) overcomes this problem by including all the cells that share a common vertex with the parent cell m, thus enlarging the computational stencil.

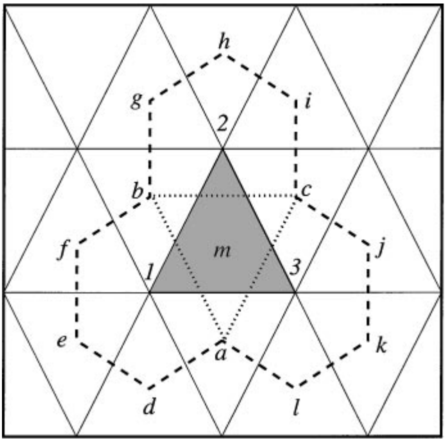

FIG. 2. Stencils for Barth & Jespersen ((i) dotted, (ii) dashed) and Frink (shaded) reconstruction procedures.

Frink [17] adopts a different strategy to increase the support of the computational stencil. In this reconstruction technique the values at all the vertices are computed by using inverse-distance-weighted averaging of the solution quantities stored at cell centers that are common to a vertex. The gradients are then computed by applying the Green–Gauss theorem to the three vertices with the path of integration being the three sides of the cell itself, as shown in Fig. 2. It has been reported [17] that this method introduces enough dissipation that oscillation-free solutions can be obtained without the use of limiters on a reasonably coarse grid for a flow field containing shocks. Furthermore, it is also cautioned in Ref. [17] that limiters may have to be used to eliminate oscillations on a sufficiently fine mesh. However, numerical experiments conducted in Section 5 reveal that even on a coarse mesh this reconstruction technique does give rise to oscillations for a discontinuous profile propagated by the two-dimensional linear convection equation.

An inverse-distance or a pseudo-Laplacian procedure is usually employed to obtain vertex values from the corresponding cell-centered values. The accuracy of the solution is reported to be less than second order when an inverse-distance method is used [18] for computing vertex values. A fully second-order-accurate method to estimate the values at the vertices using the surrounding cell-center data was presented by Holmes and Connell [19]. This new pseudo-Laplacian procedure gives most of the benefits of a true Laplacian and is also computationally inexpensive. However, for some severely distorted triangles these “optimum” weights can either become negative or become too large [19, 20]. To overcome such problems, Holmes and Connell have chosen to artificially clip the weights in the range (0, 2). It should be mentioned here that the clipping of weights, however, would result in loss of second-order accuracy, which may not be a cause for concern provided it occurs at isolated locations. This procedure for vertex values was also adopted subsequently [18] by Frink who later [20] reverted back to the inverse-distance method, when anomalous behavior was observed for Navier–Stokes computations with a pseudo-Laplacian approach, and a limiter was also employed within this framework in contrast to previous practice [17, 18]. However, for the numerical experiments reported in Section 5.3, no difficulties were encountered with a pseudo-Laplacian approach even for strongly separated flows.

An alternate procedure, which avoids involvement of vertex values for Euler computations, has been proposed by Pan and Cheng [21]. They essentially employ Barth and Jespersen’s three-point stencil in their construction but the gradient is centered owing to contributions from the three neighbors that share an interface as shown in Fig. 3. This modification increases the support of the stencil and consequently smoothens the computed gradients for highly distorted triangles, thus enhancing the stability of the overall scheme [21].

It would be instructive to compare the number of points involved in gradient computations with various methods for a grid consisting of equilateral triangles. Barth and Jespersen’s method uses 3 and 12 points for the two stencils shown in Fig. 2, whereas Frink’s method uses the additional information from the cell itself, which gives it a support of 13 points. Pan and Cheng’s method is based on a 10-point stencil, which leaves out 3 that share a vertex with the given cell as shown in Fig. 3. Having identified the support stencil and the number of points involved in computing the gradient, it would be interesting to determine whether these gradients are centered at the centroid of the cell with $O((\Delta x)^2, (\Delta y)^2)$. It should be stated that a gradient estimate of $O(\Delta x, \Delta y)$ is sufficient for second-order accuracy of the overall scheme. However, a gradient which is properly centered at the centroid for a

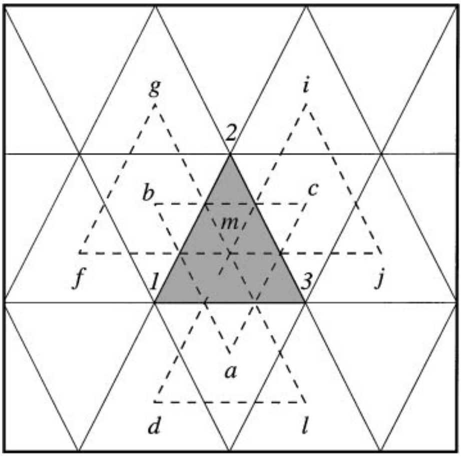

FIG. 3. Stencil for Pan and Cheng reconstruction procedure.

regular triangular grid turns out to be advantageous in mimicking a Fromm-type [22] of construction with favorable dispersion characteristics, at least for one-dimensional flows. It can be inferred (Appendix) that even for this limiting case of equilateral triangles, the x and y gradients computed using Barth and Jespersen's as well as Frink's three-point stencils are not properly centered. On the contrary, Barth and Jespersen's 12-point stencil yields a perfectly centered gradient as is the case with the new reconstruction procedure. The detailed expressions for the x and y components of the gradients can be found in the Appendix for all these methods. It should be mentioned that even for a grid consisting of equilateral triangles the number of points involved in the computation of the x and y components of the gradient are not the same for a prescribed method. The stencil used by Pan and Cheng, by virtue of contributions from the neighboring cells, also results in a perfectly centered gradient. Although perfect centering of the x and y components of the gradient, in the limiting case of equilateral triangles, is an attribute for any multidimensional reconstruction procedure it is equally important to ensure that the implementation of limiters can be readily carried out in the prescribed framework. The present reconstruction procedure has been specifically designed for compatibility with the strategy employed for the proposed three-gradient limiter.

One of the motivating factors behind the development of a new reconstruction procedure is the observation that both existing structured- as well as unstructured-grid methods use different stencils for estimating gradients for inviscid and viscous fluxes; i.e., there is no unified approach such that the total computational cost can be reduced by computing the gradients only once and using them. The new approach represents a method in which the face gradients which are necessary to compute the viscous fluxes turn out to be constituents of the cell-centered gradients needed for the inviscid fluxes.

It is well known that a gradient plane is uniquely defined by three non-collinear points. This is the starting point of the new reconstruction technique which computes gradients based on two vertices (end points of an interface) and a cell center (on either side of an interface) by looping over all the interfaces. The area-weighted average of the gradients on either side of an interface gives the x and y gradients for the face. Consider the two triangles in Fig. 4, $\triangle 13m$ and $\triangle 1a3$ for which the x and y gradients can be computed using

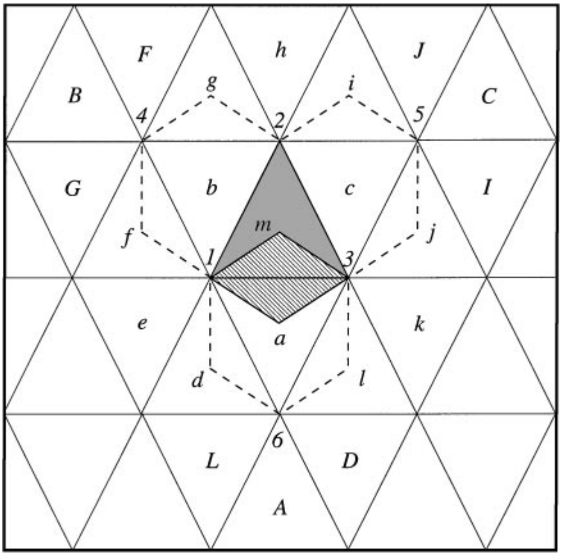

FIG. 4. Stencil for new reconstruction procedure.

the Green–Gauss theorem as

$$(W_x)_{13m} = \frac{1}{2A_{13m}}[W_1 y_{m3} + W_m y_{31} + W_3 y_{1m}] \tag{11}$$

$$(W_y)_{13m} = -\frac{1}{2A_{13m}}[W_1 x_{m3} + W_m x_{31} + W_3 x_{1m}] \tag{12}$$

$$(W_x)_{1a3} = \frac{1}{2A_{1a3}}[W_1 y_{3a} + W_3 y_{a1} + W_a y_{13}] \tag{13}$$

$$(W_y)_{1a3} = -\frac{1}{2A_{1a3}}[W_1 x_{3a} + W_3 x_{a1} + W_a x_{13}], \tag{14}$$

where $y_{m3} = y_3 - y_m$, $x_{m3} = x_3 - x_m$, and so on. The next step in obtaining the face gradient is to use the area-weighted average of these two gradients for the triangles $13m$ and $1a3$:

$$(W_x)_{1a3m} = \frac{[A_{13m}(W_x)_{13m} + A_{1a3}(W_x)_{1a3}]}{[A_{13m} + A_{1a3}]} \tag{15}$$

$$(W_y)_{1a3m} = \frac{[A_{13m}(W_y)_{13m} + A_{1a3}(W_y)_{1a3}]}{[A_{13m} + A_{1a3}]}. \tag{16}$$

Substituting Eqs. (11) and (13) in Eq. (15) and Eqs. (12) and (14) in Eq. (16) gives the expressions

$$(W_x)_{1a3m} = \frac{1}{2A_{1a3m}}\,[(W_a - W_m)y_{13} + (W_1 - W_3)y_{ma}] \tag{17}$$

$$(W_y)_{1a3m} = -\frac{1}{2A_{1a3m}}\,[(W_a - W_m)x_{13} + (W_1 - W_3)x_{ma}], \tag{18}$$

where $A_{1a3m} = A_{13m} + A_{1a3}$. These face gradients are also employed for computing the viscous fluxes for Navier–Stokes computations.

The gradient for a triangular cell is then constructed using the area-weighted average of the corresponding face gradients as follows:

$$(W_x)_m = \frac{[A_{1a3m}(W_x)_{1a3m} + A_{3c2m}(W_x)_{3c2m} + A_{2b1m}(W_x)_{2b1m}]}{[A_{1a3m} + A_{3c2m} + A_{2b1m}]} \tag{19}$$

$$(W_y)_m = \frac{[A_{1a3m}(W_y)_{1a3m} + A_{3c2m}(W_y)_{3c2m} + A_{2b1m}(W_y)_{2b1m}]}{[A_{1a3m} + A_{3c2m} + A_{2b1m}]}. \tag{20}$$

It may be noted that area weighting is carried out in Eqs. (19), (20) so that the areas which appear in the denominator in Eqs. (17), (18) (and in similar expressions for the other two faces) get cancelled out. This ensures that contributions at pair-wise common interfaces for the three faces get eliminated so that the resulting expression corresponds to a reconstruction based on a hexagonal path with three vertex and three cell-centered values traversed alternatingly.

However, the gradient for a computational cell is taken to be the area-weighted average of the gradients corresponding to its three neighbors, rather than from the above prescription, which enables limiting to be carried out straightforwardly in a framework discussed in the next section. The simplified expressions for the unlimited x and y components of the gradient for a computational cell, in the case of a grid consisting of equilateral triangles, can be found in the Appendix. It should also be mentioned that these simplifications, valid for equilateral triangles, were not introduced in Section 5 for those computations that involve unlimited gradients on an arbitrary grid.

The vertex values are computed using the pseudo-Laplacian method proposed by Holmes and Connell [19] with a slight modification regarding the clipping of weights. The clipping procedure was found to be necessary only at the boundaries since one-sided triangulation of the domain at such locations yielded unrealistic values of weights for the boundary vertices. It turns out that when the boundary vertices are shared between two or three triangles the pseudo-Laplacian procedure generates either zero or negative weights for some or all of the cells. The proposed modification involves assigning unity for the weights if they all vanish as is the case when the boundary vertex is shared between two triangles. If any weight becomes negative then its absolute value is taken for simplicity. Furthermore, the weights for the boundary vertices are clipped to prevent any of them from exceeding unity. The modification of weights, which is only carried out for the boundary vertices, is not expected to have a significant impact on accuracy since subsequent imposition of boundary conditions at these locations would weaken the effect.

4. MULTIDIMENSIONAL LIMITER

The design and development of multidimensional limiters for unstructured-grid computations has been a topic of active research in the recent past. In spite of sustained efforts by various researchers in this field, there has been very little progress in achieving consistent oscillation-removal capability in conjunction with good convergence characteristics for computations with limiters. However, all these efforts have helped in understanding the various aspects involved in the design of multidimensional limiters. The inadequacy of one-dimensional implementation of limiters on unstructured grids indicates that the limiters have to be inherently multidimensional in construction. Another desirable property of limiters is continuous differentiability, which helps in achieving smooth transition between discontinuous jumps with first-order representation and sharp but continuous gradients which require second-order consistency. Also, use of nondifferentiable functions has been shown to adversely affect the convergence of the solution to steady state in most of the cases.

Barth and Jespersen [9] were the first to propose a multidimensional limiter for Euler computations on unstructured grids. This popular and the most widely used limiter has been shown to stall the convergence to steady state [13], which could be due to the use of nondifferentiable functions such as max and min, apart from clipping smooth extrema [23]. Venkatakrishnan's modification [13] helps in improving the convergence characteristics of the original limiter, which, however, comes at the expense of compromising on monotonicity. Also, the convergence seems to be strongly influenced by a parameter, which controls the degree of limiting, that is a function of an estimate of average grid size and an arbitrary constant chosen by conducting a few numerical experiments for each problem. The need for such user interactions makes it difficult for the limiter to be applied for large general-purpose solvers. Another modification was attempted by Aftosmis *et al.* [14] who observed that Barth and Jespersen's limiter attenuates the gradient in all directions equally and suggested its directional implementation. Even though this approach reduces the inherent dissipation in the limiter, it fails to provide satisfactory results.

Since the convergence problems can be largely attributed to the use of nondifferentiable functions, it would be advantageous to employ differentiable limiters that have proved to be quite successful with structured-grid computations. The van Albada limiter, apart from being continuously differentiable, has the additional attractive property of not clipping smooth extrema. Earlier attempts to implement the van Albada limiter on unstructured grids in a one-dimensional framework have failed [4, 23] to yield results which are relatively insensitive to the grid. This indicates that for unstructured-grid computations, a limiter has to be multidimensional in construction apart from being differentiable. It can be seen from the work of Van Rosendale [24] that a three-gradient extension of the van Albada limiter can be readily constructed based on a straightforward generalization.

For a two-dimensional triangular unstructured grid, the limited gradient within a cell can be obtained by taking the weighted average of three representative gradients,

$$\nabla W_m^l = \omega_a \nabla W_a + \omega_b \nabla W_b + \omega_c \nabla W_c, \tag{21}$$

where ω_a, ω_b, and ω_c are the weights given by the multidimensional limiter function and ∇W_a, ∇W_b, and ∇W_c are the three unlimited gradients which are combined to produce the limited gradient ∇W_m^l. The choice of these three gradients plays a crucial role in limiting convergence as well as in obtaining a good-quality solution which is relatively insensitive to grid perturbations and connectivity.

Van Rosendale's choice was inspired by the representation of the larger of Barth and Jespersen's stencil (Fig. 2). The gradient obtained from this stencil can be interpreted as being the area-weighted average of the gradients at the three vertices of a cell as computed by applying the Green–Gauss theorem to the surrounding cell-center data. This procedure essentially reverses the sequence of operations employed by Frink in which vertex values are computed first and then the Green–Gauss theorem, applied to the three vertex values, provides the gradient for a cell. After computing the gradients ∇W_1, ∇W_2, and ∇W_3 at the three vertices of the cell m, Van Rosendale obtains the weights which are functions of the three unlimited gradients. The weights corresponding to the van Albada limiter [24] are

$$\omega_1(g_1, g_2, g_3) = \frac{(g_2g_3 + \epsilon^2)}{(g_1g_2 + g_2g_3 + g_3g_1 + 3\epsilon^2)} \tag{22}$$

$$\omega_2(g_1, g_2, g_3) = \frac{(g_1g_3 + \epsilon^2)}{(g_1g_2 + g_2g_3 + g_3g_1 + 3\epsilon^2)} \tag{23}$$

$$\omega_3(g_1, g_2, g_3) = \frac{(g_1g_2 + \epsilon^2)}{(g_1g_2 + g_2g_3 + g_3g_1 + 3\epsilon^2)}, \tag{24}$$

where g_1, g_2, and g_3 are functions of the three vertex gradients involved in the limiting process and can be chosen as the square of the L_2 norm, i.e., $g_1 = \|\nabla W_1\|_2^2$, $g_2 = \|\nabla W_2\|_2^2$, and $g_3 = \|\nabla W_3\|_2^2$, which is a computationally efficient choice. Furthermore, ϵ is a small number which is introduced to prevent indeterminacy, caused by the vanishing of the three gradients, in regions of uniform flow. The constraints on the weights for second-order consistency require each of them to become $1/3$ when the three gradients are equal. The weights are homogeneous of degree 0 so that the limited gradient turns out to be homogeneous of degree 1 to ensure that the units of measurement scale out linearly. In addition, symmetry with respect to pair-wise interchange of gradients requires

$$\omega_1(g_1, g_2, g_3) = \omega_2(g_2, g_1, g_3) = \omega_3(g_3, g_2, g_1). \tag{25}$$

The limited gradient using Van Rosendale's procedure can be obtained by replacing the gradients for a, b, and c in Eq. (21) by those corresponding to the vertices 1, 2, and 3. It may be recalled that the one-dimensional van Leer limiter is the harmonic average of two differences, the forward and backward. In some sense this multidimensional limiter, which is referred to as a van Albada limiter in [24], can also be regarded as a van Leer limiter because it turns out to be a harmonic average for each of the two components of the gradient vector, with appropriately prescribed weights, provided the three values involved are positive. It should, however, be noted that the weights for the two components of the limited gradient vector are the same in Eq. (21), which is the formulation employed in the present research.

Several numerical experiments showed that this multidimensional limiter, which possesses the property of not clipping smooth extrema, performs well for most of the flow problems considered but fails to completely remove oscillations at discontinuities for a few of them (Section 5) in an implementation quite different from that of Van Rosendale [24]. This led to the development of a new multidimensional limiter, which has been shown to be consistently effective in removing oscillations and has excellent convergence characteristics in addition to not clipping smooth extrema. It involves the prescription for the weights as

$$\omega_a(g_a, g_b, g_c) = \frac{(g_bg_c + \epsilon^2)}{\left(g_a^2 + g_b^2 + g_c^2 + 3\epsilon^2\right)} \tag{26}$$

$$\omega_b(g_a, g_b, g_c) = \frac{(g_ag_c + \epsilon^2)}{\left(g_a^2 + g_b^2 + g_c^2 + 3\epsilon^2\right)} \tag{27}$$

$$\omega_c(g_a, g_b, g_c) = \frac{(g_ag_b + \epsilon^2)}{\left(g_a^2 + g_b^2 + g_c^2 + 3\epsilon^2\right)}, \tag{28}$$

where $g_a = \|\nabla W_a\|_2^2$, $g_b = \|\nabla W_b\|_2^2$, and $g_c = \|\nabla W_c\|_2^2$. Even though this modification in the weights may appear minor the implementation of the procedure differs significantly from that of Van Rosendale [24] in the choice of gradients for constructing the limiter; this is the primary reason for introducing different subscripts for g in Eqs. (22)–(24) as compared to Eqs. (26)–(28). Instead of the three vertex gradients chosen for limiting in [24], an implementation appropriate to the flow physics inherent in a MUSCL finite-volume formulation forms the basis for prescribing the three gradients in the present case. Since each cell interacts with its neighbor through the common interface, the cell-centered gradients of the three neighboring cells should be a more relevant choice for limiting and are used in the present work in all test cases including those involving the van Albada limiter. The resulting stencil from this nonoverlapping construction is shown in Fig. 4. The unlimited gradient for a cell is taken to be the area-weighted average of its three neighboring cell gradients, ensuring cancellation at common interfaces as the result of contiguity, which is an important requirement fulfilled by the present hexagon-based reconstruction procedure.

Care must be exercised in choosing the third gradient at the boundary where two different approaches can be used for the limited as well as unlimited construction. To maintain consistency with the nonoverlapping construction, one can use a face gradient for the boundary interface. Alternatively, to make it somewhat similar with the interior representation the cell-centered gradient for the boundary cell can be employed, which makes the construction an overlapped one. Numerical experiments show that these two constructions at the boundary do not make much of a difference insofar as the solutions are concerned.

The implementation of the new limiter is straightforward since, after computing the cell-centered gradients in all cells, limiting can be carried out for each cell in the domain, which requires the unlimited gradients of its three immediate neighbors. The limited gradient ∇W_m^l then replaces the unlimited gradient ∇W_m in Eq. (8) to get the higher-order-accurate limited values of W.

5. RESULTS AND DISCUSSIONS

The following numerical experiments are aimed at assessing the accuracy of the new reconstruction technique for a variety of problems and testing the effectiveness of the new limiter in removing the numerical oscillations that occur in the neighbourhood of shocks without stalling the convergence to steady state. It should be mentioned that limiters have been deployed actively without recourse to any freezing [13] strategy in all the computations. Furthermore, ϵ^2, which is a small number introduced to prevent indeterminacy in the weights for the limiter, has been set to be 10^{-10} in all numerical experiments reported here. Laminar Navier–Stokes computations for separated flows have been carried out to demonstrate the feasibility of a unified formulation for inviscid and viscous fluxes.

5.1. *Two-Dimensional Linear Wave Equation*

Consider the two-dimensional wave equation

$$u_t + \nabla \cdot \mathbf{F} = 0 \tag{29}$$

with $\mathbf{F}(u; \mathbf{a}) = u\mathbf{a}$ representing the flux vector and $\mathbf{a}$ being the constant wave velocity. The upwind flux at an interface is given by

$$f(u_\mathrm{L}, u_\mathrm{R}) = \begin{cases} \mathbf{F}(u_\mathrm{L}; \mathbf{a}) \cdot \mathbf{n} & \text{if } \mathbf{a} \cdot \mathbf{n} \geq 0 \\ \mathbf{F}(u_\mathrm{R}; \mathbf{a}) \cdot \mathbf{n} & \text{otherwise.} \end{cases} \tag{30}$$

Here **n** is the unit normal vector pointing from left (L) to right (R) for an oriented interface. In a first-order-accurate computation, only cell-centered values are used for the left and right states. Higher-order-accurate interface values are obtained from Eq. (8) with the cell-centered gradient computed using Frink's method apart from the new reconstruction procedure as described in Section 4. In this transient computation, second-order temporal accuracy is achieved by the two-stage Hancock [11] procedure

$$u_m^{n+1/2} = u_m^n - \frac{\Delta t}{2\mathcal{A}_m} \sum_k \mathbf{F}\left(u_m^n + \nabla u_m^n \cdot \mathbf{r}\right) \cdot \mathbf{n} \tag{31}$$

$$u_m^{n+1} = u_m^n - \frac{\Delta t}{\mathcal{A}_m} \sum_k \mathbf{F}\left(u_m^{n+1/2} + \nabla u_m^n \cdot \mathbf{r}, u_k^{n+1/2} + \nabla u_k^n \cdot \mathbf{r}\right), \tag{32}$$

where $\mathcal{A}_m$ is the area of the computational cell and the summation is to be carried out over the three bounding interfaces. This time-integration procedure has also been employed in Ref. [25] to study the behavior of various limited reconstruction techniques as applied to Eq. (29) for the convection of a square discontinuity, as chosen in the present example, and a double sine profile.

The entire computational domain, defined by $-1 \leq x, y \leq +1$, is composed of right-triangular cells constructed from a uniform structured grid in two different ways with anisotropic or isotropic connectivity; the resulting unstructured grid types are referred to as A and B, respectively. Grid A is obtained from the square cells by locally joining the top-left to bottom-right corner as in [25] whereas grid B is generated by requiring that each of the four neighboring squares that share an edge has diagonals oriented opposite to that prescribed for any cell. Thus half of the interior vertices for grid B would be located at the intersections of four interfaces and the remaining half would have eight interfaces, whereas for grid A all the interior vertices are connected to six interfaces. It has been recently shown [26] that limiters which strongly depend upon grid connectivity encounter difficulties for convection on grid B, which results in catastrophic loss of accuracy as reflected by first-order degradation of even L_1 error norms. It should be noted that in the pattern of connectivity which has been prescribed here, grid B is the same but grid A has diagonals oriented opposite to that of Ref. [26]. The convection velocity is prescribed to be $\mathbf{a} = (1, 2)^T$ as in Ref. [26] so that the initial profile is convected from bottom-left to top-right direction, making an angle of about 63° with respect to the positive x axis, with periodicity imposed to permit reentry. It should be noted that the convection direction is neither aligned with any of the interfaces of a computational cell nor aligned with their normals. The time step Δt is determined by choosing a constant mesh ratio of 0.1, i.e., $\Delta t/l = 0.1$, where $l = \sqrt{2\mathcal{A}_m}$ is the spacing between two successive vertices in the x or y direction. The cell-averaged value, which is obtained by analytically integrating the prescribed initial profile within the triangular cell, forms the initial condition for each of the grid types; this is also the exact solution at a time when the convected distribution returns to its starting location.

Two initial profiles, a square discontinuity and a doubly raised cosine which has a steep but continuous gradient, are used, respectively, as test cases to determine the oscillation-removing capability and accuracy of the limiters. The results are presented when the convected profile first returns to its original position and the carpet as well as the contour plots are for the coarsest grid, corresponding to $l = 0.0333$. A grid-refinement study has been conducted for the doubly raised cosine with the slopes, obtained from the plots of L_1, L_2, and L_∞ errors against $l(= \Delta x = \Delta y)$ for grids A and B, indicating the order of accuracy on each of these two grid types.

5.1.1. Square discontinuity. The square discontinuity, defined between $-1 \le x, y \le +1$, has the following functional form:

$$u(x, y) = \begin{cases} 1 & \text{if} -0.5 \le x, y \le +0.5 \\ 0 & \text{otherwise.} \end{cases} \tag{33}$$

The carpet as well as the contour plots of this initial profile, which is also the exact solution after convection, are shown in Figs. 5a,c for grid A and Figs. 6a,c for grid B. The first-order-accurate scheme on grid A is highly dissipative and smears out the discontinuity completely, as inferred from Fig. 5b with a noticeable anisotropy induced by the grid clearly evident in Fig. 5d. However, convection on grid B largely preserves isotropy of the initial profile, as revealed by the contour plot in Fig. 6d, even though the first-order-accurate scheme is relatively less dissipative for this grid type.

The next step is to test higher-order-accurate methods without limiters to determine the extent of oscillations encountered with the new method of evaluating the gradient, which is centered in the limiting case of an equilateral triangulation, so that comparisons can be established on an anisotropic grid consisting of right-angled triangles with Frink's method. Figures 7a–d show carpet and contour plots obtained on grid A with Frink's as well as the new method. It can be seen that Frink's method produces larger overshoots and

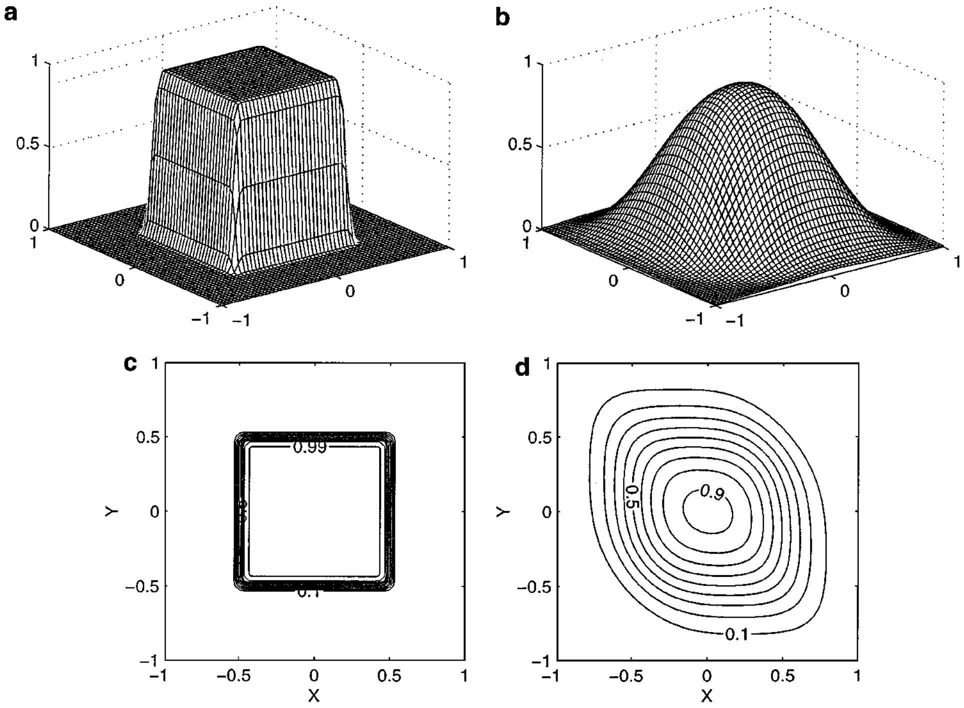

FIG. 5. Carpet and contour plots for the exact and first-order-accurate solutions of a square discontinuity on grid type A. (a, c) exact solution; (b, d) first-order-accurate solution.

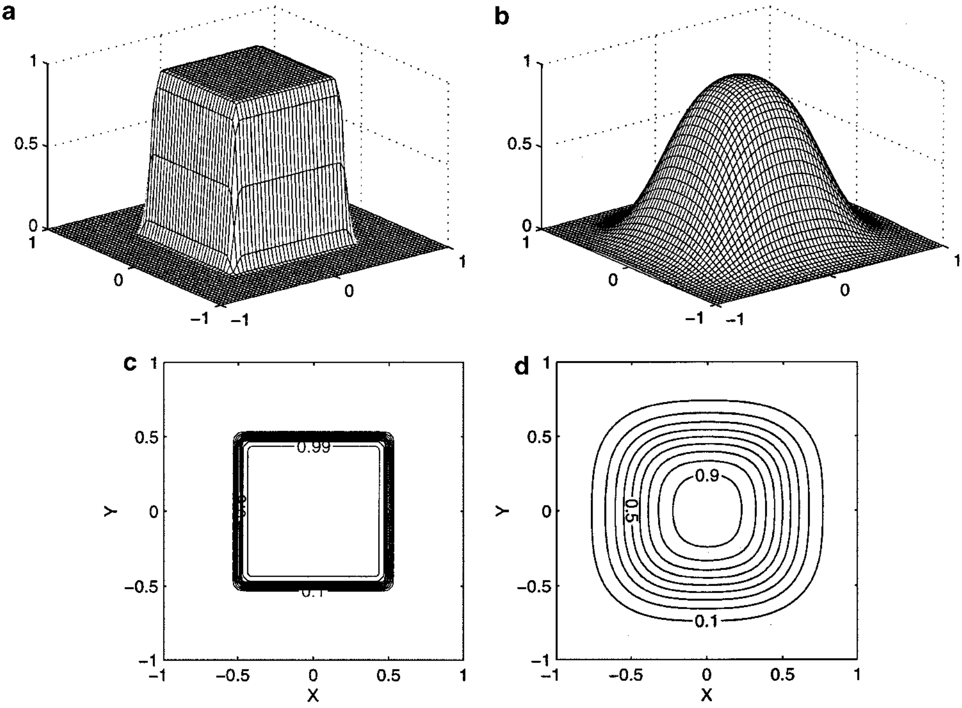

FIG. 6. Carpet and contour plots for the exact and first-order-accurate solutions of a square discontinuity on grid type B. (a, c) exact solution; (b, d) first-order-accurate solution.

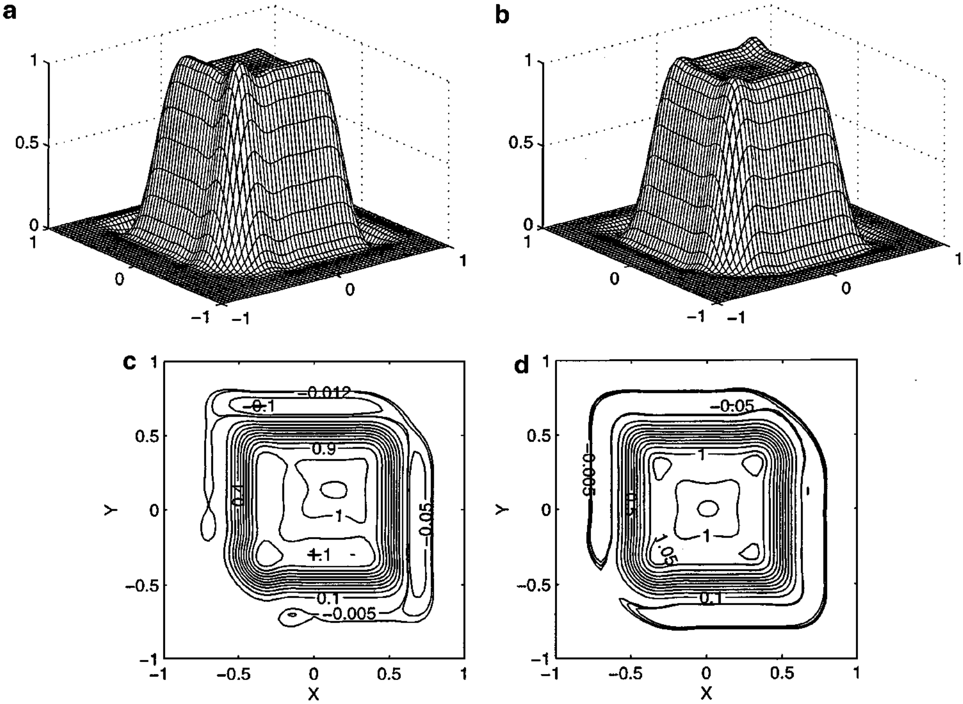

FIG. 7. Carpet and contour plots of a square discontinuity with Frink (a, c) and new unlimited (b, d) reconstruction procedures on grid type A.

TABLE I
Maximum and Minimum Values for the Square Discontinuity

	First order		Frink		Unlimited		van Albada		New limiter	
l	Max	Min	Max	Min	Max	Min	Max	Min	Max	Min
					Grid A					
0.0333	0.939	0.002	1.225	−0.119	1.113	−0.061	1.005	−0.002	1.000	0.000
0.0167	0.994	0.000	1.250	−0.133	1.116	−0.063	1.004	−0.001	1.000	0.000
0.0111	0.999	0.000	1.267	−0.141	1.117	−0.064	1.004	−0.001	1.000	0.000
0.0083	1.000	0.000	1.278	−0.148	1.119	−0.066	1.003	−0.001	1.000	0.000
					Grid B					
0.0333	0.979	0.000	1.221	−0.136	1.121	−0.067	1.020	−0.013	1.000	0.000
0.0167	0.999	0.000	1.244	−0.151	1.127	−0.072	1.020	−0.013	1.000	0.000
0.0111	1.000	0.000	1.260	−0.161	1.130	−0.075	1.020	−0.013	1.000	0.000
0.0083	1.000	0.000	1.270	−0.168	1.134	−0.079	1.021	−0.014	1.000	0.000

undershoots as compared to the new method. Furthermore, the new method performs better in preserving the symmetry of the initial profile and maintains the extent of oscillation at a uniform level. A similar conclusion holds for convection on grid B and the plots have not been shown. However, the maximum and minimum values for convection on grids A and B are presented in Table I for different grid spacings, which leads to the conclusion that the new method produces less oscillations even on a fine grid than Frink's method on a coarse grid. It can also be observed that convection on grid B with the new method yields slightly larger magnitudes of extrema, for a prescribed grid spacing, compared to those on grid A. This is also the case with Frink's method for the minima but the trend is reversed for the maxima. However, these results confirm the need for limiters even though Euler results [17, 18] with Frink's method without limiters apparently do not reveal oscillations in the neighborhood of shocks whereas limiters were employed subsequently [20] for three-dimensional Navier–Stokes computations. In the present study the application of limiters has been restricted to the new procedure for gradient estimation since the proposed implementation of limiters cannot be extended straightforwardly to Frink's construction.

The van Albada limiter fails to completely remove oscillations on grids A as well as B, which is evident from the values listed in Table I. The extent of oscillations, being small, is not clearly represented in Figs. 8a and 9a, which contain the carpet plots for the two grid types, but the corresponding contour plots in Figs. 8c and 9c reveal some distortions at the peak and traces of undershoots. The new limiter does not produce any oscillations upon grid refinement as observed from Table I with Figs. 8d and 9d, for grid types A and B, which show the contours to be nearly symmetric and free from distortions. Closer examination of Figs. 8d and 9d reveals barely perceptible anisotropy of the convected profile on grid A relative to grid B. This is in contrast to the significant anisotropy found in the results presented for the square discontinuity on grid A in Ref. [25] for the Durlofsky *et al.* [27] or MLG (maximum limited gradient) procedures for limiting. It should also be noted that the new limiter resolves the intersection of discontinuities at the four corners, significantly better than any of the limiters tested in Ref. [25]. The spikes are much more pronounced at the four corners as inferred from the carpet plot of Fig. 7b for the unlimited case.

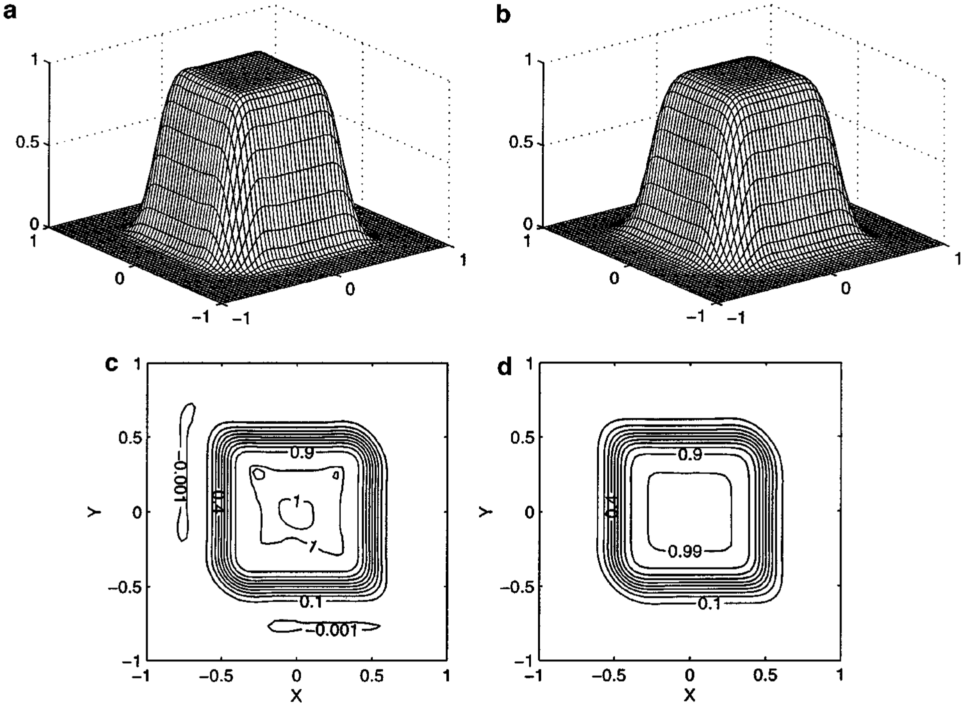

FIG. 8. Carpet and contour plots of a square discontinuity with new reconstruction procedure on grid type A. (a, c) van Albada and (b, d) new limiter.

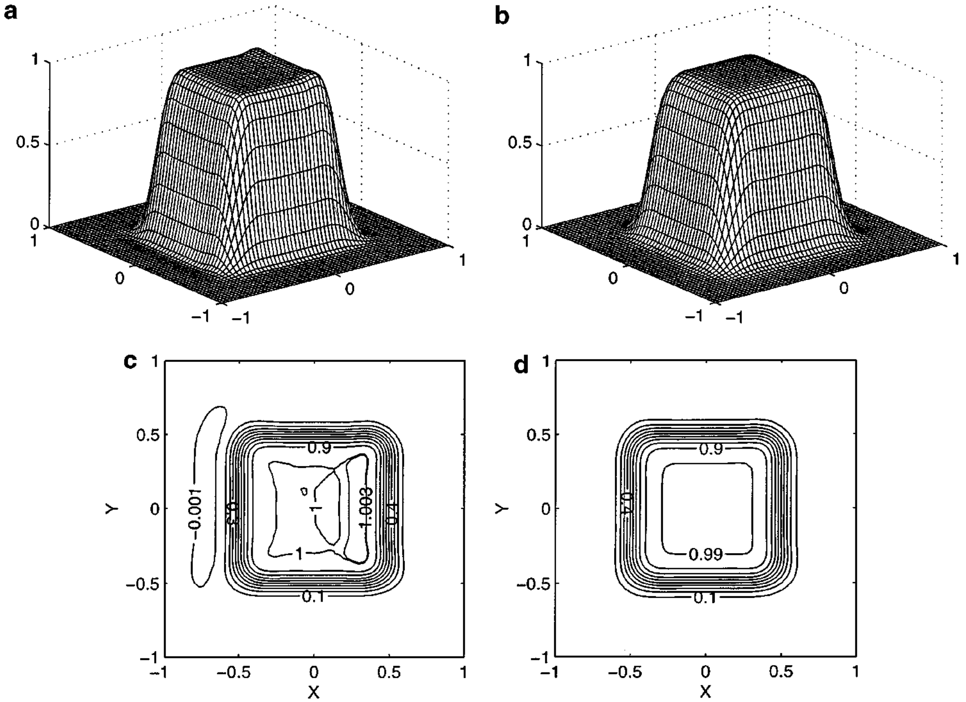

FIG. 9. Carpet and contour plots of a square discontinuity with new reconstruction procedure on grid type B. (a, c) van Albada and (b, d) new limiter.

TABLE II

Maximum and Minimum Values for the Doubly Raised Cosine

	First order		Frink		Unlimited		van Albada		New limiter	
l	Max	Min	Max	Min	Max	Min	Max	Min	Max	Min
					Grid A					
0.0333	0.475	0.000	0.983	−0.020	0.976	−0.010	0.930	0.000	0.876	0.000
0.0167	0.644	0.000	0.997	−0.008	0.996	−0.004	0.975	0.000	0.950	0.000
0.0111	0.731	0.000	0.999	−0.005	0.999	−0.002	0.986	0.000	0.971	0.000
0.0083	0.784	0.000	1.000	−0.003	0.999	−0.001	0.991	0.000	0.981	0.000
					Grid B					
0.0333	0.540	0.000	0.990	−0.020	0.987	−0.010	0.955	−0.001	0.916	0.000
0.0167	0.711	0.000	0.998	−0.008	0.998	−0.004	0.985	0.000	0.967	0.000
0.0111	0.790	0.000	0.999	−0.005	0.999	−0.002	0.992	0.000	0.981	0.000
0.0083	0.836	0.000	1.000	−0.003	1.000	−0.001	0.995	0.000	0.988	0.000

The next step is to calculate the order of accuracy of the new reconstruction with and without the new limiter. More importantly it is the ability of a limiter not to clip the smooth extrema which will ensure its versatility. This can be easily verified by convecting a smooth profile which has a sharp peak. The profile used for this purpose is a doubly raised cosine defined subsequently with its peak value 1 occurring at $x = y = 0$ of the computational domain. Compared to the double sine employed in [25–27], this has the advantage of having one peak and it covers only a portion of the computational domain so that any oscillations that might occur at the base of the profile can be readily detected.

5.1.2. Doubly raised cosine. The doubly raised cosine function, defined between $-1 \leq x, y \leq +1$, is

$$u(x, y) = \begin{cases} \frac{1}{4}[1 + \cos(2\pi x)][1 + \cos(2\pi y)] & \text{if } -0.5 \leq x, y \leq +0.5 \\ 0 & \text{otherwise.} \end{cases} \tag{34}$$

Carpet and contour plots for the convection of doubly raised cosine profile have not been shown since anisotropy introduced by grid topology or convection direction could not be visibly observed and the extent of undershoots, being very small, are better represented as entries in Table II, which also contains peak values; Fig. 10 and Table III indicate the orders

TABLE III

Orders of Accuracy

	Grid A			Grid B		
	L_1	L_2	L_∞	L_1	L_2	L_∞
First Order	0.67	0.61	0.63	0.80	0.73	0.73
Unlimited	2.53	2.33	1.81	2.11	2.01	1.69
Frink	2.05	1.90	1.53	1.95	1.85	1.43
van Albada	2.43	2.19	1.45	2.05	2.02	1.51
New Limiter	2.19	1.92	1.32	2.09	1.94	1.36

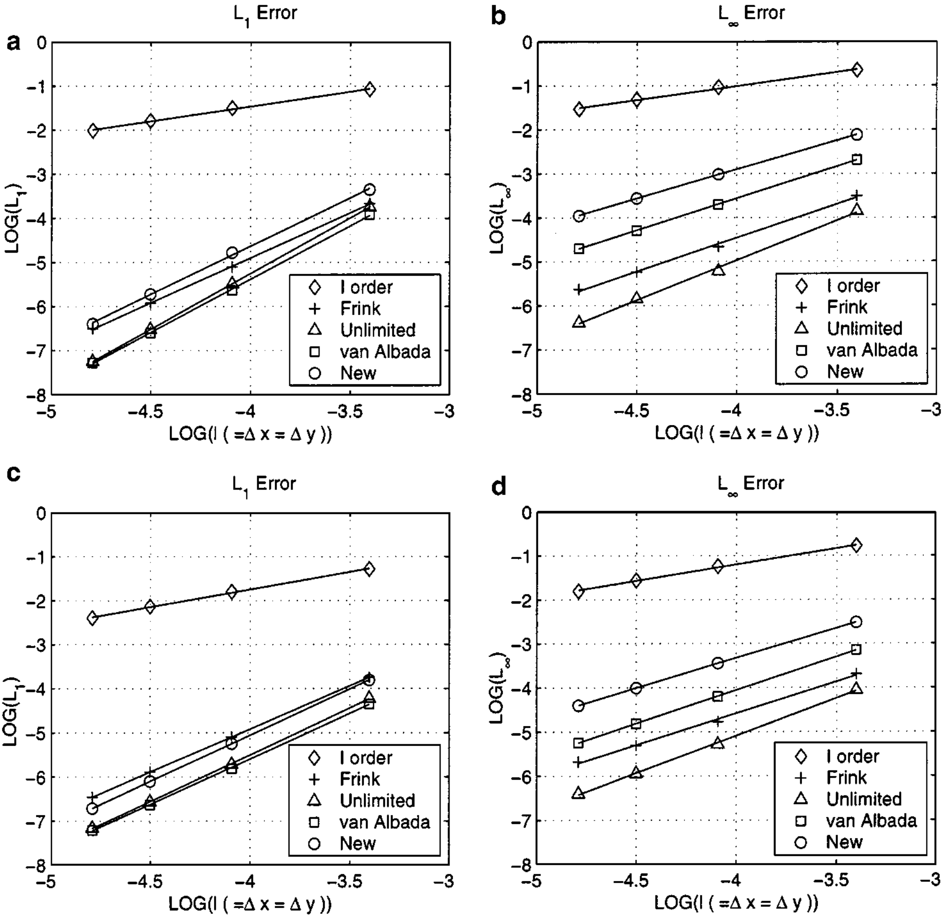

FIG. 10. Log–log plots of L_1 and L_∞ errors versus l ($= \Delta x = \Delta y$) for doubly raised cosine on grid types A (a, b) and B (c, d).

of accuracy of different procedures on both grid types as obtained from this grid-refinement study.

It can be observed from Table II that the first-order-accurate scheme predictably diffuses the profile, with grid B being better than grid A at preserving peak values, which is also true for all higher order schemes. Also, the peak values obtained with the new reconstruction even without limiters is slightly less than that obtained from Frink's method, which is one of the disadvantages of employing a wider stencil, but this difference can be seen to vanish upon grid refinement. Frink's method exhibits discernible undershoots with the extent being almost twice that obtained with the new reconstruction procedure as inferred from Table II. It should also be noted from Table II that the magnitude of undershoots reduces with grid refinement as expected for a continuous profile, in contrast to that for the square discontinuity in Table I. The introduction of limiters in the new reconstruction procedure removes the oscillations except that the van Albada limiter produces a mild undershoot for the coarsest grid of type B. The limiters also do not clip the smooth extremum, which will be reflected in the L_∞ norms of the errors obtained from a grid-refinement study carried out next.

The slopes in Table III indicate the order of accuracy of each scheme as obtained from plots of L_1, L_2, and L_∞ errors against l as in Fig. 10, where the plot for L_2 error has not been included owing to space constraints. It is clear that the two limiters preserve second-order accuracy of the new reconstruction procedure in L_1 and L_2 norms but not in the L_∞ norm, as anticipated, because of the extremum present in the initial profile. The slopes indicate the new gradient reconstruction procedure with limiters is globally second-order accurate and that the local error is between first and second order. It is particularly noteworthy that the sensitivity to grid connectivity between types A and B, with loss of accuracy on the latter reported in Ref. [26] for various limited schemes, has been effectively reduced by the present high-resolution procedure, which is intrinsically endowed with a dependence on a wide computational stencil.

5.2. *Two-Dimensional Euler Equations*

In this section, the accuracy of the proposed reconstruction procedure and the oscillation-removing ability of the new limiter is assessed in conjunction with the van Albada limiter based upon well-documented numerical experiments for inviscid flows. Osher's numerical-flux function, which is continuously differentiable, has been employed to ensure that the influence of limiters on convergence characteristics can be isolated effectively. Steady-state Euler as well as Navier–Stokes solutions are obtained with an explicit time-integration procedure using a six-stage Runge–Kutta technique [28].

5.2.1. Inviscid flow past a NACA 0012 airfoil. Three different test cases are used to evaluate the performance of the reconstruction procedure and the limiter for the two-dimensional inviscid compressible flow past a NACA 0012 airfoil from AGARD [29] and GAMM [30] workshops. The parameters correspond to two transonic flows and a subsonic flow for which the free-stream Mach number and angle of attack are: (i) $M_\infty = 0.80$, $\alpha = 1.25^\circ$; (ii) $M_\infty = 0.85$, $\alpha = 1^\circ$; and (iii) $M_\infty = 0.63$, $\alpha = 2^\circ$. Test cases (i) and (ii) are characterized by the presence of shock waves on both upper and lower surfaces and it is necessary to compute the flows with limiters to avoid numerical oscillations that may occur in their neighborhood. Most of the unstructured-grid computations reported in the literature use solely test case (i), which has a relatively strong shock on the upper surface and a weak shock on the lower surface. Test case (ii) is more demanding as far as the limiters are concerned because both shocks are strong. Furthermore, the shocks are preceded by a fairly large near-constant region and the limiters are expected to encounter problems [13] in resolving this abrupt transition. Test case (iii) is a smooth flow without any shock waves and hence it does not require the use of limiters. However, it would be desirable to determine whether the limiters clip the smooth extremum occurring in the surface-pressure distribution for Euler computations, which have been performed with and without limiters.

Four different triangular meshes have been used to compute the flows described by the test cases (i)–(iii). The first one, which is referred to as structured-triangulated grid (STRI), is obtained from a structured 128×32 O-grid by joining the diagonals as depicted in Fig. 11a, which contains 8192 cells in the computational domain. Figure 11b shows a perturbed grid, which is obtained by randomly perturbing the structured-triangulated grid everywhere except at inner and outer boundaries. It can be thought of as an intermediate stage between a structured-triangulated grid and a genuinely unstructured one. Figures 11c,d show genuinely unstructured grids, which have been generated as in Ref. [31] using the Bowyer–Watson algorithm based on a Delaunay triangulation technique. Unstructured grid 1 (USG1) in

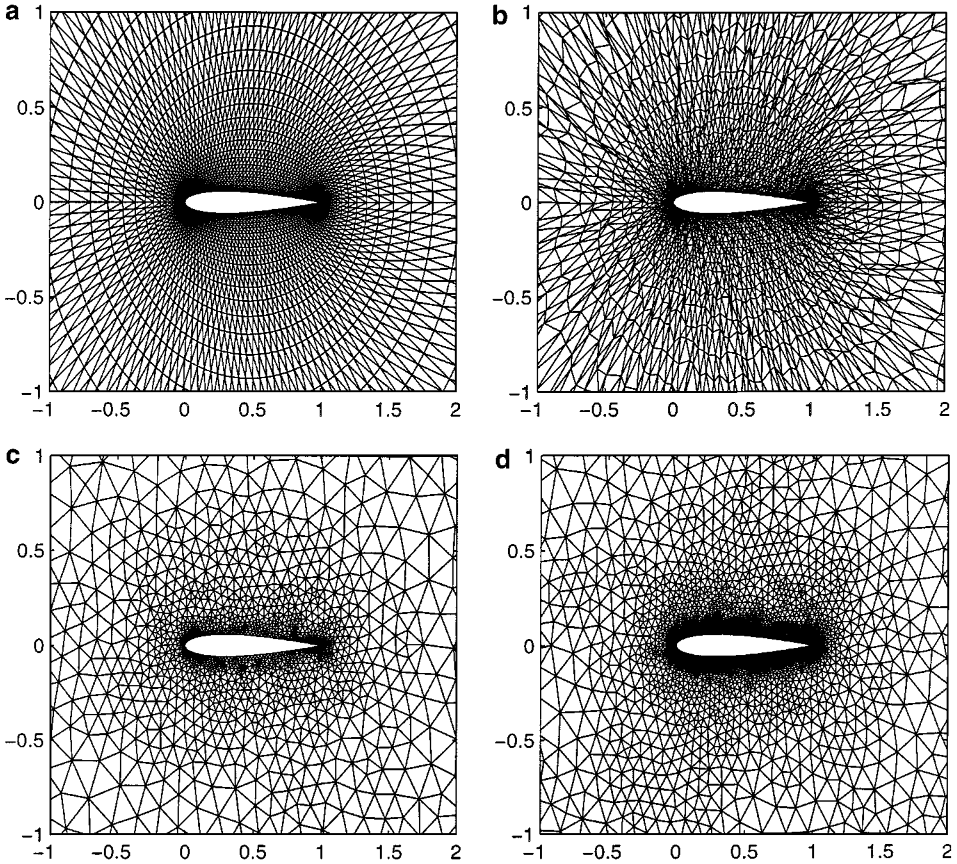

FIG. 11. Grids used for Euler computations. (a) Structured triangulated grid; (b) perturbed grid; (c) unstructured grid 1 (USG1); (d) unstructured grid 2 (USG2).

Fig. 11c has 128 points on the airfoil (similar to the structured-triangulated and perturbed grids) and 4360 cells in the computational domain, whereas the unstructured grid 2 (USG2) in Fig. 11d has 512 points on the airfoil surface and 12,858 cells in the computational domain, which is the finest grid used for Euler computations in the present work. The outer boundary for all these grids is a circle located 12 chord lengths away from the airfoil.

One set of ghost points are generated for imposition of higher-order-accurate boundary conditions, by reflecting the cell-centered locations of those cells with an interface abutting the boundaries. Although computation of inviscid fluxes requires pressure alone to be prescribed at the boundaries, the gradient estimation for these boundary cells requires two components of velocity and specific volume to be prescribed at the ghost points. At the solid wall, zero normal velocity is prescribed and the other quantities are computed from the interior using the corresponding cell-center values and one-sided gradients. At the outer boundary, an asymptotic far-field solution consisting of a lifting flow about the airfoil is imposed as in Ref. [32].

Figure 12 shows the coefficient of pressure (C_p) distributions on the airfoil for the test cases (i) and (ii) computed on unstructured grid USG1, which are compared with structured grid results from Ref. [16]. In order to establish meaningful comparisons both the grids have 128 points on the airfoil and approximately equal number of cells in the computational

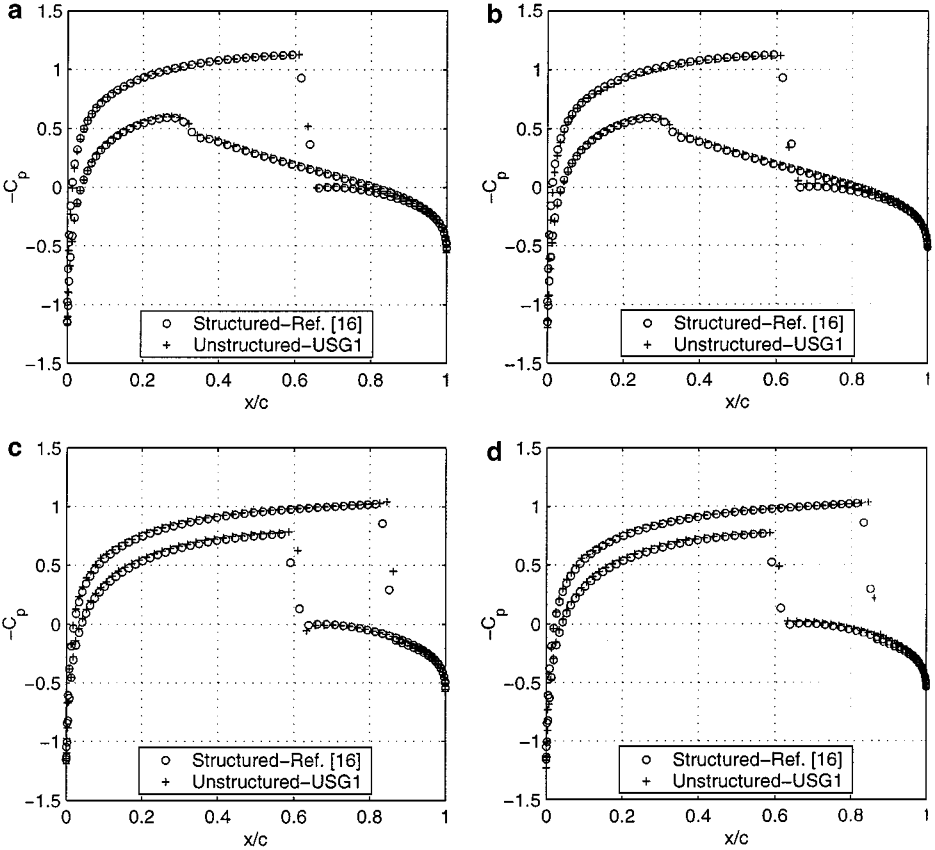

FIG. 12. Comparison of surface-pressure distributions on structured (Ref. [16]) and unstructured grids for NACA 0012 transonic cases. (a) van Albada, $M_\infty = 0.8, \alpha = 1.25°$; (b) new limiter, $M_\infty = 0.8, \alpha = 1.25°$; (c) van Albada, $M_\infty = 0.85, \alpha = 1.0°$; (d) new limiter, $M_\infty = 0.85, \alpha = 1.0°$.

domain. Furthermore, the two solutions have been obtained using Osher's scheme. It should be mentioned that a standard van Albada limiter based on a locally one-dimensional representation was used in Ref. [16] whereas both a multidimensional van Albada limiter and the new limiter have been employed in the present computations. The solutions on the unstructured grid in Fig. 12 reveal sharp shock-capturing ability of the proposed high-resolution procedure and the shock locations compare favorably with those of the reference solutions on a structured grid. It can be observed that the multidimensional van Albada limiter and the new limiter are very effective in suppressing oscillations within the framework of the new reconstruction procedure, which yield pressure distributions on USG1 in remarkable agreement with the structured-grid results of Ref. [16]

Figure 13 shows the performance of the van Albada and the new limiter for the test cases (i) and (ii) on structured-triangulated and perturbed grids. As stated earlier, both the grids contain the same number of cells and the latter is obtained from the former by merely relocating the points randomly. This random perturbation of the grid has a noticeable impact on the effectiveness of the multidimensional van Albada limiter. For test case (i), the van Albada limiter produces an overshoot for the structured-triangulated grid whereas the oscillation is completely removed on the perturbed grid, which can be seen from Figs. 13a,b.

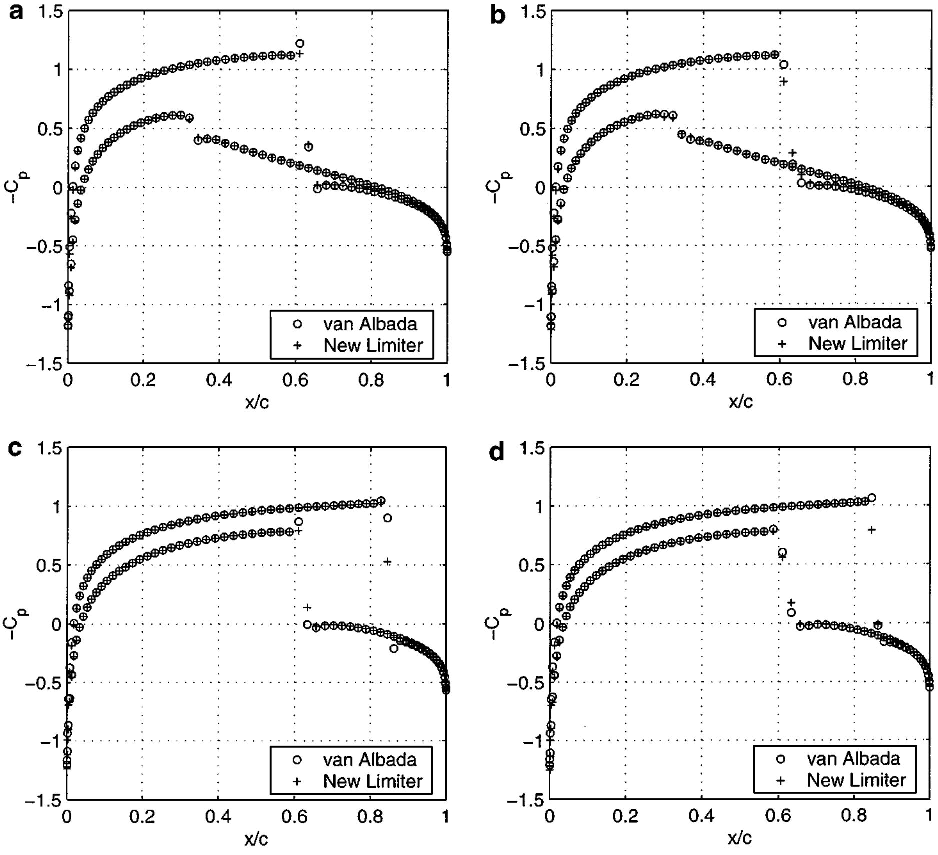

FIG. 13. Surface-pressure distributions with van Albada and new limiters on structured–triangulated and perturbed grids for NACA 0012 transonic cases. (a) structured-triangulated grid, $M_\infty = 0.8, \alpha = 1.25°$; (b) perturbed grid, $M_\infty = 0.8, \alpha = 1.25°$; (c) structured-triangulated grid, $M_\infty = 0.85, \alpha = 1.0°$; (d) perturbed grid, $M_\infty = 0.85, \alpha = 1.0°$.

For test case (ii), the van Albada limiter leaves a pronounced spike on the lower surface for the structured-triangulated grid. The random perturbation of the grid has apparently helped in reducing the extent of oscillation on the lower surface for the van Albada limiter whereas it seems to have slightly exacerbated the small upturning on the upper surface. This clearly indicates that the van Albada limiter is sensitive to the grid used and may not be consistently effective in removing oscillations at discontinuities. However, the new limiter is successful in yielding oscillation-free solutions for all the cases considered. It should be mentioned that Frink's method was also employed for these test cases, and the C_p distributions, which are not shown here, yielded nearly the same extent of oscillations as with the van Albada limiter.

The convergence histories for test cases (i) and (ii) for the structured-triangulated grid and for USG1 are presented in Fig. 14. The L_∞ norm of the residual, summed over the four nondimensional conservation equations, has been reduced by 10 orders of magnitude, and the residue histories, which are plotted for every iteration, reveal a steady fall after 5 orders of magnitude for all cases without exhibiting any tendency to stall. The initial oscillatory convergence, present in limited as well as unlimited residue histories during a reduction of nearly five orders of magnitude, are typical manifestations of transonic flow computations in which the shocks tend to oscillate about their steady-state locations before settling down.

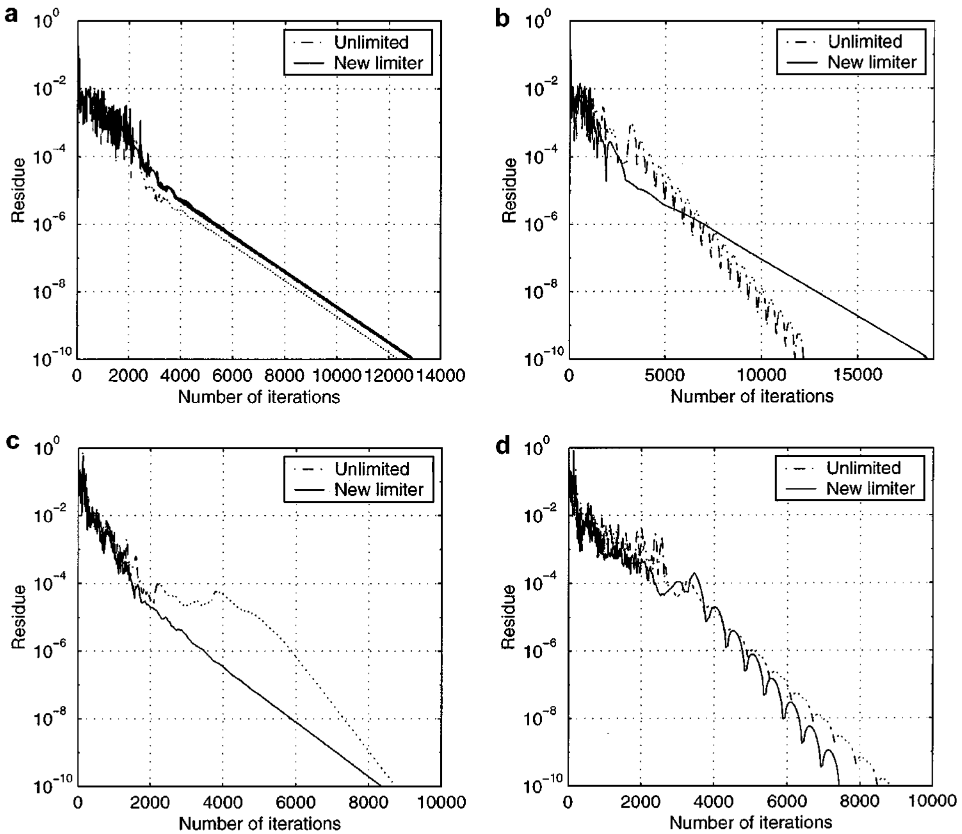

FIG. 14. Convergence characteristics of new limiter on structured-triangulated and unstructured grid 1 for NACA 0012 transonic cases. (a) structured-triangulated grid, $M_\infty = 0.8, \alpha = 1.25°$; (b) structured-triangulated grid, $M_\infty = 0.85, \alpha = 1.0°$; (c) unstructured grid: USG1, $M_\infty = 0.8, \alpha = 1.25°$; (d) unstructured grid: USG1, $M_\infty = 0.85, \alpha = 1.0°$.

Similar behavior was also observed for the other grids considered and the plots have not been included because of space constraints.

The iso-Mach contours for the test cases (i) and (ii) on structured-triangulated grids and USG1, based on results obtained with the new limiter, are shown in Fig. 15. For test case (i), the upper surface shock is cleanly captured on both grids whereas the presence of the weak shock on the lower surface is hardly discernible in Figs. 15a,b owing to uniform spacing of contours. This weak shock is more clearly represented in the corresponding surface-pressure distributions in Figs. 12 and 13. However, for test case (ii), the shock waves on both upper and lower surfaces of the airfoil in Figs. 15c,d are quite clear; they impinge normal to the surface and are free from distortions.

It is significant to study the behavior of the limiters on a fine grid where the dissipation due to the grid is reduced to a low level. Figure 16 shows the performance of the van Albada limiter and the new limiter on USG2. The extent of oscillations in the unlimited case and the action of limiters are clearly brought out here. In the case of strong shocks, where the limiter needs to be much more active for the removal of pre-shock oscillations, an undesirable consequence is that a post-shock Zierep singularity is attenuated significantly; however, it is encouraging to note that for test case (i) this effect is benign for the weak shock

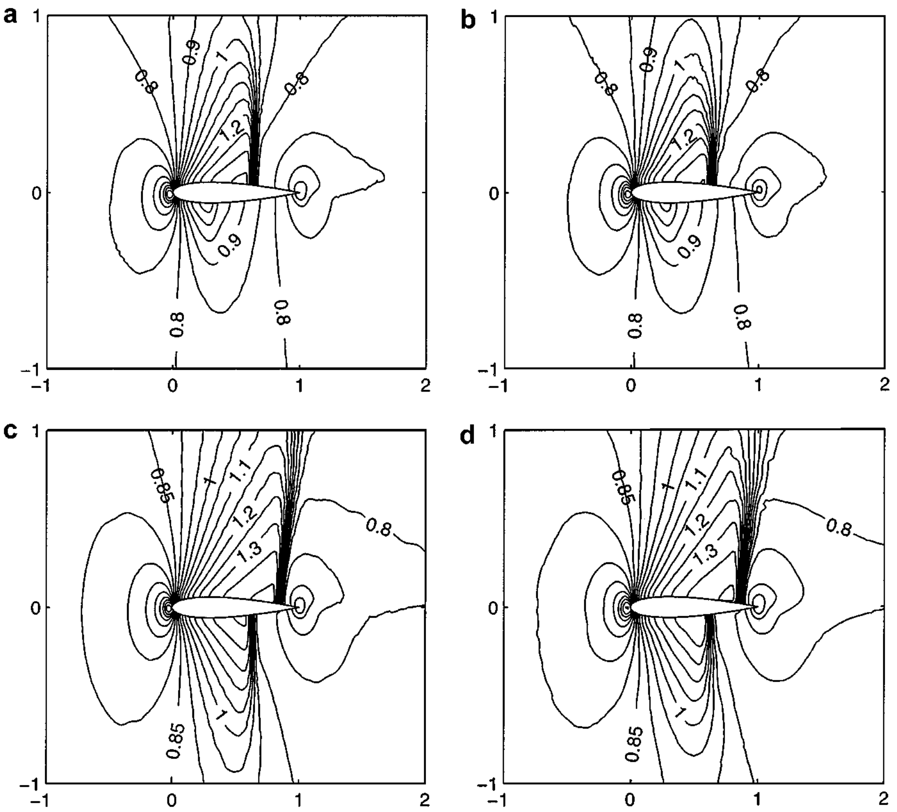

FIG. 15. Iso-Mach contours for solutions on structured-triangulated and unstructured grid 1 for NACA 0012 transonic cases. (a) structured-triangulated grid, $M_\infty = 0.8, \alpha = 1.25°$; (b) unstructured grid: USG1, $M_\infty = 0.8, \alpha = 1.25°$; (c) structured-triangulated grid, $M_\infty = 0.85, \alpha = 1.0°$; (d) unstructured grid: USG1, $M_\infty = 0.85, \alpha = 1.0°$.

on the lower surface. The advantages of unstructured grids, even for a simple configuration, become evident upon comparing the number of computational cells in USG2 with those employed in Ref. [33] for fine-grid computations of test case (i) based upon structured grids.

The lift and drag coefficients (C_l and C_d) for test cases (i) and (ii) obtained with the van Albada and the new limiter are compared in Table IV with the reference values [29]

TABLE IV
Reference and Computed Lift and Drag Coefficients for NACA 0012 Inviscid Transonic Cases

	$M_\infty = 0.8, \alpha = 1.25°$		$M_\infty = 0.85, \alpha = 1°$	
Parameter	C_l	C_d	C_l	C_d
AGARD [29]	0.36320	0.02300	0.37930	0.05760
Structured [16]: 128 × 32	0.35495	0.02255	0.37992	0.05464
USG1—van Albada	0.34795	0.02435	0.36969	0.05902
USG1—New Limiter	0.34452	0.02696	0.37704	0.06067
USG2—van Albada	0.35083	0.02426	0.38364	0.05854
USG2—New Limiter	0.35161	0.02421	0.37371	0.05889

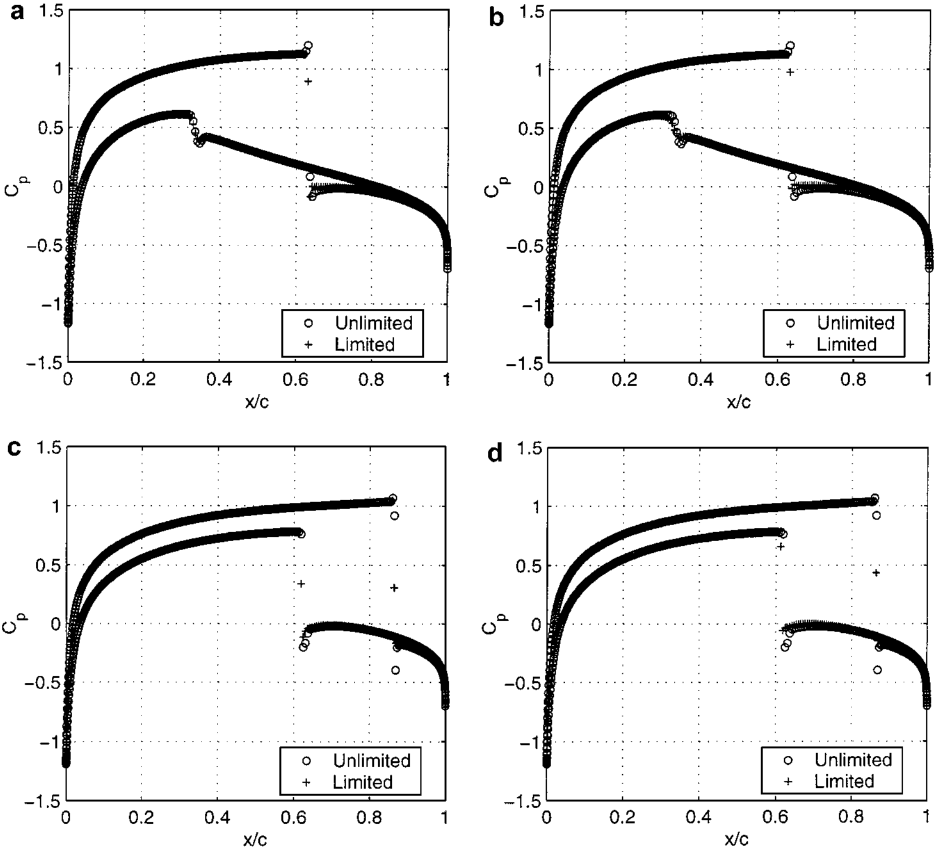

FIG. 16. Surface-pressure distributions with van Albada and new limiters on unstructured grid 2 for NACA 0012 transonic cases. (a) USG2: van Albada, $M_\infty = 0.8$, $\alpha = 1.25°$; (b) USG2: new limiter, $M_\infty = 0.8$, $\alpha = 1.25°$; (c) USG2: van Albada, $M_\infty = 0.85$, $\alpha = 1.0°$; (d) USG2: new limiter, $M_\infty = 0.85$, $\alpha = 1.0°$.

and the structured-grid results from Ref. [16] corresponding to Osher's scheme. It can be inferred that the unstructured-grid values, based on the proposed high-resolution procedure, compare favorably with those obtained on a structured grid having nearly the same number of computational cells.

An important aspect of a limiter, which will make it uniformly applicable, is its ability to preserve smooth extrema encountered in Euler computations. Figure 17 shows computed C_p distributions for the shock-free test case (iii) obtained on the grids shown in Fig. 11 in that order. It is clearly seen that the new limiter does not clip the smooth extremum and the pressure distribution is not significantly altered even in the regions of large gradients. The lift and drag coefficients for this test case (iii) on USG1 and USG2 are compared with the reference values and the structured-grid data [16] in Table V. It can be seen that there is not much variation in C_l for the cases considered. The drag coefficients, being small in magnitude, reveal a greater degree of sensitivity to the grid and also to the limiter.

5.2.2. Inviscid flow past a staggered-biplane configuration. The primary advantage of unstructured grids is their ability to straightforwardly account for multiple bodies in the flow. One of the popular test cases that is used for the purpose of demonstrating complex flow arising from interaction effects of multiple bodies is the staggered biplane. It comprises two

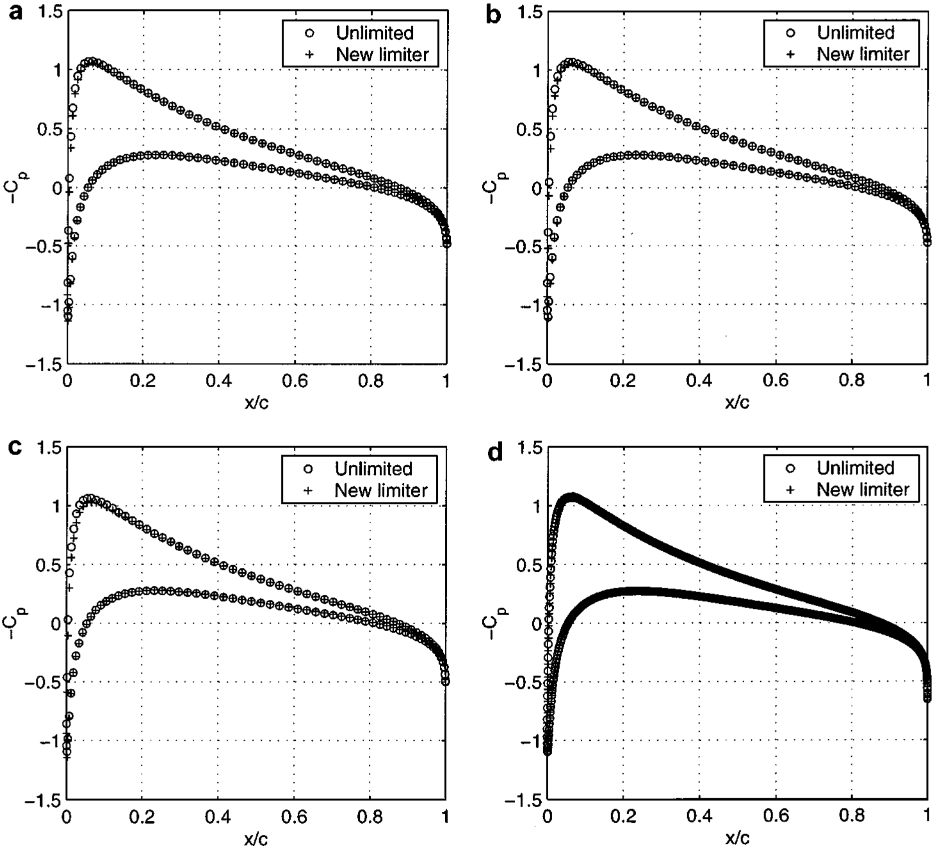

FIG. 17. Surface-pressure distributions without limiter and with new limiter for NACA 0012 subsonic case on various grids. $M_\infty = 0.63$; $\alpha = 1.25°$. (a) structured-triangulated grid; (b) perturbed grid; (c) USG1; (d) USG2.

NACA 0012 airfoils, staggered by half a chord length in the pitchwise as well as chordwise direction. The resulting configuration yields a combination of internal as well as external flow as shown in Fig. 18a, which depicts the unstructured grid generated with 256 points on each airfoil and with 6718 cells in the computational domain. The Mach number chosen is 0.7 with the flow being parallel to the chord of the airfoils. Under these conditions an isolated NACA 0012 airfoil will yield a shock-free flow field whereas in the case of the

TABLE V
Reference and Computed Lift and Drag Coefficients for NACA 0012 Inviscid Subsonic Case

Parameter	C_l	C_d
AGARD [29]	0.33350	0.00003
Structured—Unlimited [16]	0.33372	0.00017
STRI—Unlimited	0.32842	0.00079
USG1—Unlimited	0.32560	0.00202
USG2—Unlimited	0.33198	0.00054
USG1—New Limiter	0.31815	0.00561
USG2—New Limiter	0.32850	0.00219

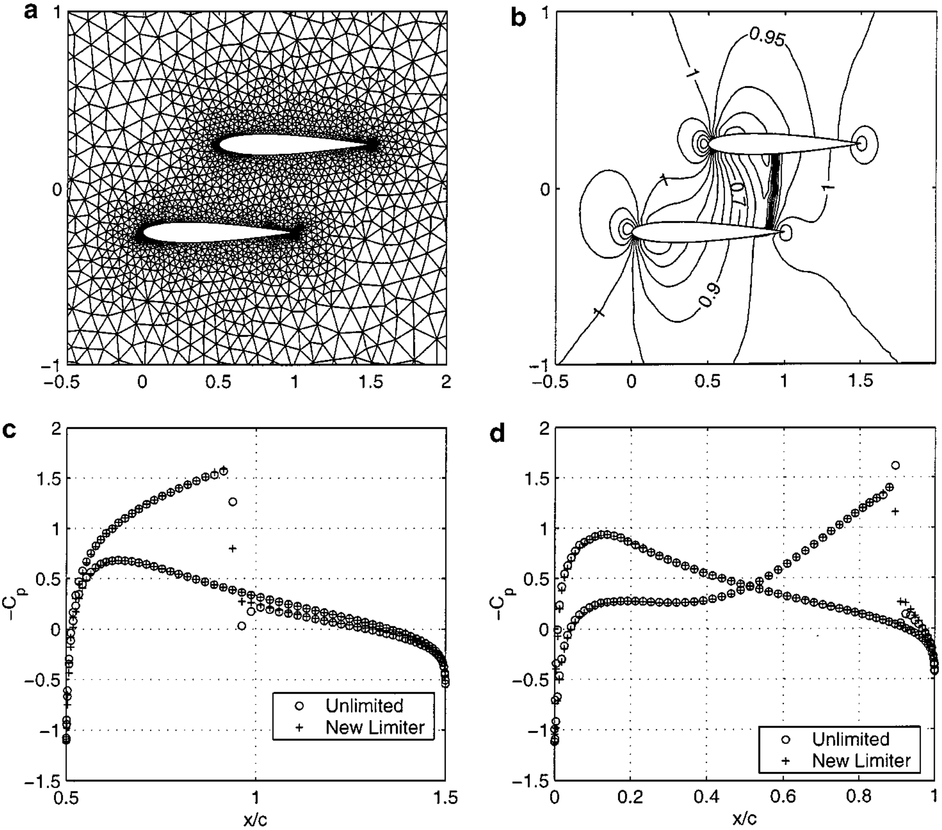

FIG. 18. Inviscid-flow ($M_\infty = 0.7$, $\alpha = 0^\circ$) solution for staggered biplane. (a) close-up view of grid; (b) pressure contours; (c) upper airfoil C_p; (d) lower airfoil C_p.

staggered-biplane configuration the region between the airfoils acts as a channel which accelerates the flow. As a result of this flow confinement a strong normal shock is formed near the channel exit, which is captured accurately in Fig. 18b, and the isobars shown compare well with those in the literature [34–39]. The C_p distributions on both the airfoils for unlimited and with the new limiter are plotted in Figs. 18c,d. The pressure distribution on the upper surface of the lower airfoil shows a spike at the shock for the unlimited case, which is effectively removed by the new limiter. No convergence difficulty was observed for this case even for a reduction in the residual up to 10 orders of magnitude.

5.3. *Two-Dimensional Navier–Stokes Solutions*

The numerical examples reported in this section demonstrate the ability of the new reconstruction procedure to compute viscous flows on genuinely unstructured grids. Navier–Stokes solutions are obtained using Osher's flux-difference splitting scheme for the convective fluxes whereas the viscous fluxes are based on face gradients computed at an interface. It should be recalled that the higher-order-accurate procedure, based on the new reconstruction strategy, readily provides face gradients for the viscous fluxes as an intermediate construction, which yield formulae similar to Eqs. (15) and (16) at each interface, resulting in a unified formulation.

Boundary conditions are prescribed through the use of ghost cells at all the boundaries. At a solid wall, no-slip and isothermal wall boundary conditions are imposed to compute the two components of velocity and temperature, respectively. The wall temperature is taken to be the free-stream total temperature. Pressure is extrapolated from the interior by computing the higher-order-accurate value at the wall using a one-sided gradient. For all the viscous computations, the outer boundary is a circle located 50 chord lengths from the geometric center of the airfoil. Free-stream values are prescribed as far-field boundary conditions. All Navier–Stokes solutions have been converged up to 10 orders of magnitude reduction in L_∞ norm of the residual, summed over the four nondimensional conservation equations.

5.3.1. Viscous flow past a NACA 0012. Viscous computations for flow past a NACA 0012 airfoil have been performed for two different flow parameters: (i) $M_\infty = 0.8$, $\alpha = 10°$, $\text{Re}_\infty = 500$ and (ii) $M_\infty = 0.5$, $\alpha = 0°$, $\text{Re}_\infty = 5000$. The low-Reynolds-number test case (i) is well documented [40] in the GAMM workshop on compressible Navier–Stokes computations. The significance of this flow stems from the presence of a large separated region on the upper surface of the airfoil. The objective is to demonstrate the ability of the new reconstruction procedure to accurately resolve this complex flow feature on genuinely unstructured grids. To establish a comparison, results have also been obtained on a 160×50 structured-triangulated grid (STRI-V).

The unstructured grid (USG-V) with 512 points on the airfoil contains 24,686 cells in the computational domain, whose close-up view in Fig. 19a indicates the uniform clustering near the surface of the airfoil. The main feature of the flow, a prominent vortex that extends over 50% of the chord on the upper surface, as computed on the genuinely unstructured

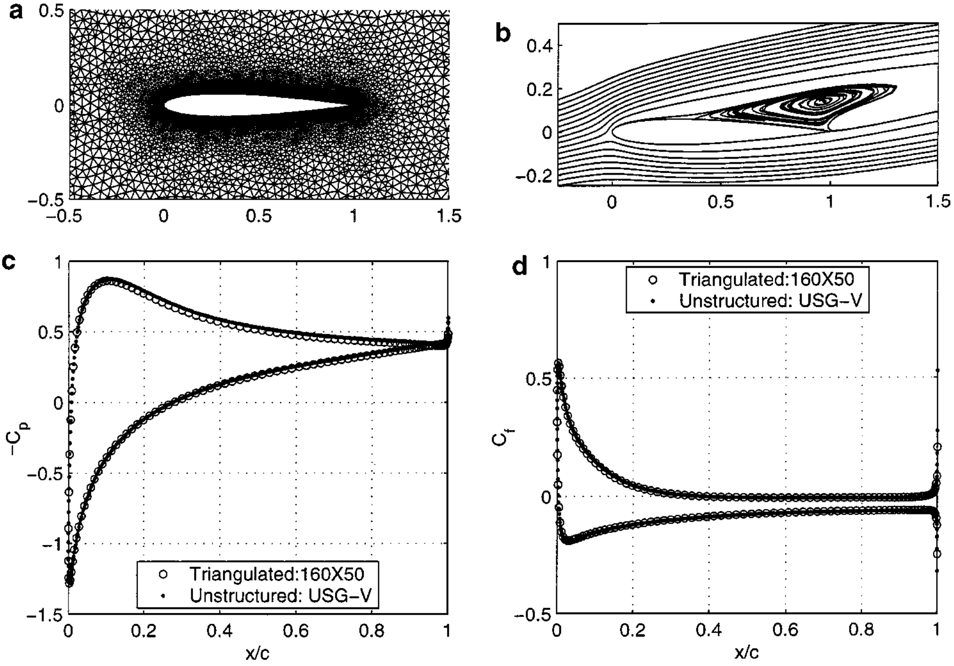

FIG. 19. Viscous-flow ($M_\infty = 0.8$, $\alpha = 10°$, $\text{Re}_\infty = 500$) solution for NACA 0012 airfoil on genuinely unstructured grid. (Note: $-C_\text{f}$ has been plotted for the lower surface.) (a) near-field view of grid; (b) streamlines; (c) pressure distribution; (d) skin-friction distribution.

TABLE VI
Reference and Computed Lift and Drag Coefficients for NACA 0012 Viscous Case i ($M_\infty = 0.8$, $\alpha = 10°$, $\mathrm{Re}_\infty = 500$)

Parameter	C_{d_p}	C_{d_f}	$C_{\mathrm{d}_{\mathrm{total}}}$	$C_{\mathrm{l}_{\mathrm{total}}}$
USG-V	0.15287	0.12439	0.27726	0.50231
STRI-V	0.14930	0.12286	0.27216	0.49394
GAMM [30]	—	—	0.243–0.2868	0.4145–0.517

grid, is clearly shown in Fig. 19b and compares well with that reported in [41]. These streamlines also match those (not shown) obtained on STRI-V. The surface-pressure and skin-friction distributions in Figs. 19c,d compare the solutions obtained on these two grids. The overall profiles are similar to those reported in literature [40]. It should be noted that the C_p and C_f distributions computed on the genuinely unstructured grid are smooth and are indistinguishable from structured-triangulated ones. This is also reflected in the total (sum of pressure and skin-friction components) lift and drag coefficients given in Table VI. The C_l and C_d values obtained on USG-V and STRI-V are close to each other and are well within the range reported in the GAMM workshop [40].

Most of the computations reported in literature, other than some in [40], follow either a hybrid semi-structured grid, structured-triangulated grid [41–45], or an adapted unstructured grid [46] for NACA 0012 airfoil computations. In the present work, however, a genuinely unstructured grid (USG-V) has been shown to produce results which are in good agreement with those obtained on a structured-triangulated grid (STRI-V). It should be pointed out that to accurately resolve the boundary layer, the size of the cell in a direction normal to the boundary layer should be adequately small. In the case of structured-quadrilateral grids, and also structured-triangulated grids derived from them, the “height” of the cells can be controlled by varying the clustering independent of the “width” of the cells as defined by the distribution of points on the airfoil. However, the unstructured-grid-generation program employed in the present work generates near-equilateral triangles and as a result it becomes necessary to choose more points on the surface of the airfoil, in order to generate cells of smaller size, which leads to a noticeable increase in the total number of cells in the computational domain. However, the accuracy of results obtained combined with the suitability of unstructured grids for complex geometries offsets this small penalty one has to pay for the use of a genuinely unstructured grid, even though it is possible to judiciously control the total number of cells by reducing the number of cells in the far-field region. A better grid-generation procedure based on the advancing-front method [47] would be able to achieve a more refined control in the near-field region as required for viscous flow simulations.

The second example, for the flow $M_\infty = 0.5, \alpha = 0°$, $\mathrm{Re}_\infty = 5000$ past a NACA 0012 airfoil, is considered a difficult test problem since the Reynolds number is near the upper limit for steady laminar flow [42, 44]. The results are computed on structured grid STRI-V alone because it was observed that the initially symmetric flow appeared to exhibit a mild asymmetry at this Reynolds number. The close-up view of structured-triangulated grid STRI-V, obtained from a perfectly symmetric structured grid which has been constructed by reflection about its chord, is shown in Fig. 20a. The streamlines in Fig. 20b near the trailing edge of the airfoil show slightly asymmetric vortices on either side of the $y = 0$

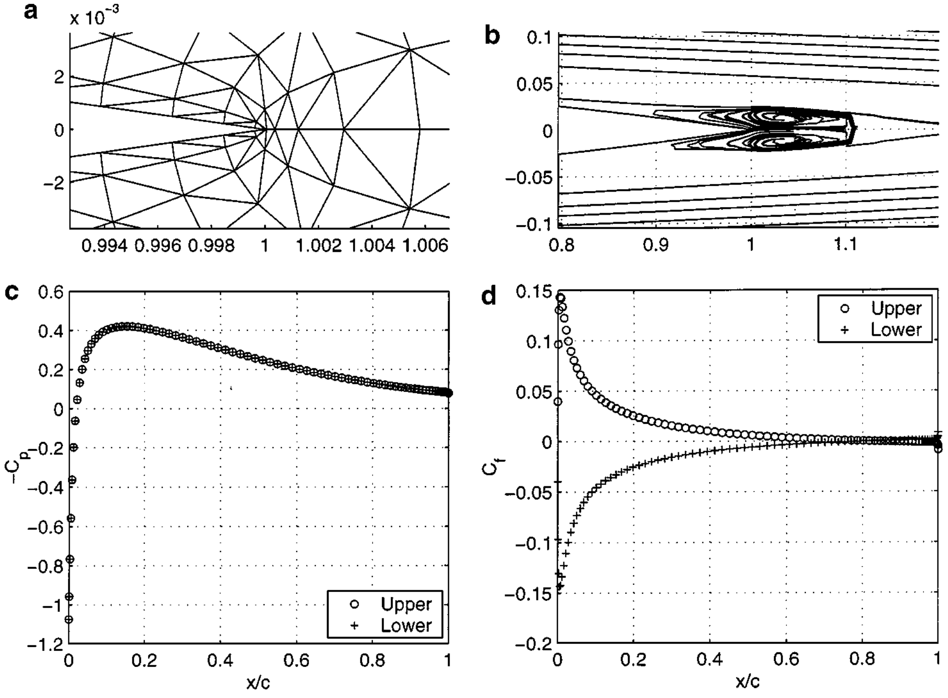

FIG. 20. High-Reynolds-number viscous-flow ($M_\infty = 0.5$, $\alpha = 0°$, $\mathrm{Re}_\infty = 5000$) solution for NACA 0012 airfoil on structured–triangulated grid. (Note: $-C_\mathrm{f}$ has been plotted for the lower surface.) (a) near-field view of grid; (b) streamlines; (c) pressure distribution; (d) skin-friction distribution.

axis. The cause for this asymmetry has not been identified and is beyond the scope of this investigation; it should be mentioned that the asymmetry disappeared upon significant reduction of the Reynolds number. However, the pressure and skin-friction distributions shown in Figs. 20c,d appear symmetric. This may be due to the fact that the vortices are located some distance away from the surface of the airfoil and the cores are just behind the trailing edge. The lift coefficient, reported in Table VII, turns out to be zero. The drag coefficients match well with those reported in the literature [48–50].

5.3.2. Viscous flow past a staggered-biplane configuration. To further demonstrate the capabilities of the new reconstruction procedure, the flow past a complicated geometry, as in the case of a staggered NACA 0012 biplane configuration, has been chosen for performing viscous flow computations. The grid, whose near-field view is shown in Fig. 21a, contains

TABLE VII

Reference and Computed Lift and Drag Coefficients for NACA 0012 Viscous Case ii (M_∞ = 0.5, α = 0°, Re_∞ = 5000)

Parameter	C_{d_p}	C_{d_f}	$C_{\mathrm{d}_{\mathrm{total}}}$	$C_{\mathrm{l}_{\mathrm{total}}}$
STRI-V	0.02285	0.03272	0.05557	0.0000
Venkatakrishnan [48]	0.02300	0.03268	0.05568	—
Radespiel and Swanson [49]	0.02235	0.03299	0.05534	—
Crumpton *et al.* [50]	0.02260	0.03350	0.05610	—

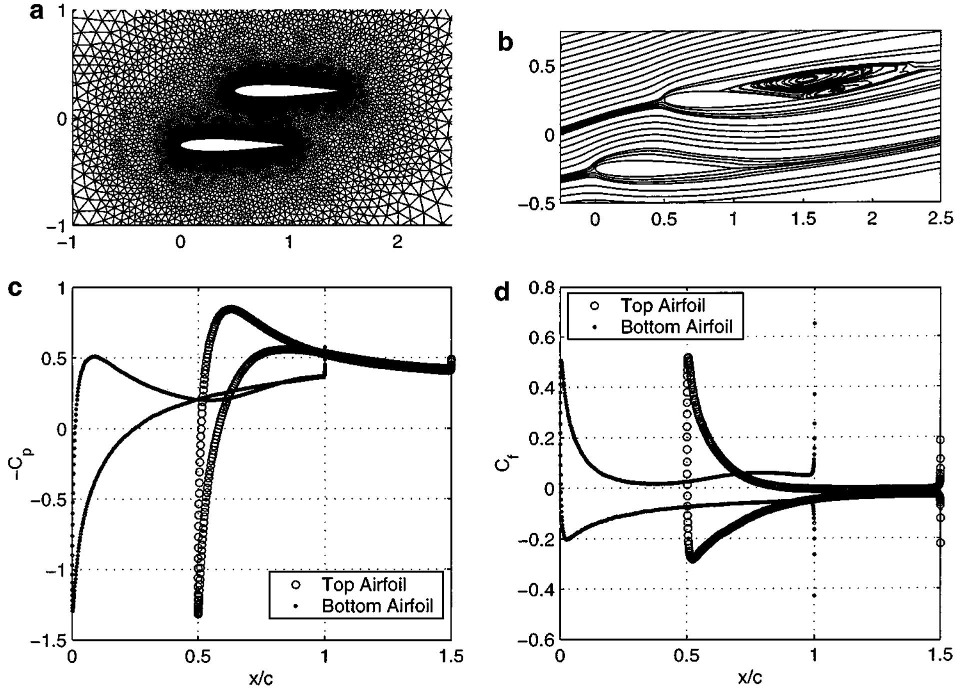

FIG. 21. Viscous-flow ($M_\infty = 0.8, \alpha = 10^\circ, \mathrm{Re}_\infty = 500$) solution for staggered biplane. (Note: $-C_\mathrm{f}$ has been plotted for lower surfaces.) (a) near-field view of grid; (b) streamlines; (c) pressure distribution; (d) skin-friction distribution.

512 points on each airfoil with 23,232 triangular cells in the computational domain. The streamlines corresponding to the flow parameters $M_\infty = 0.8, \alpha = 10^\circ$, and $\mathrm{Re}_\infty = 500$ are shown in Fig. 21b. These flow conditions are the same as those for test case (i) involving an isolated NACA 0012 airfoil. The separated region on the upper surface of top airfoil, as shown in Fig. 21b, reveals two vortices. The secondary vortex apparently is introduced by the addition of a bottom airfoil, which is evident by comparing Figs. 19b and 21b. The pressure and skin-friction distributions for the two airfoils have been plotted in Figs. 21c,d. Although no experimental data or reference solutions are available for this test case, plausible viscous-flow features have been captured with the high-resolution unstructured-grid procedure.

6. CONCLUSIONS

A high-resolution procedure has been developed for Euler and Navier–Stokes computations on unstructured grids. It involves a gradient-reconstruction procedure devised for implementation within a multidimensional framework for a three-gradient limiter. Numerical experiments confirm the oscillation-removal capability of the proposed limiter, although this has not been proven rigorously, and its favorable convergence characteristics without one having to resort to freezing [13, 51] or any such palliative. A distinctive feature of this multidimensional limiter is that it exploits the gradient vector in determining the largest variation rather than explicitly employing the largest and the smallest values at the three vertices, as computed based on the unlimited gradient within a computational cell, in the limiting process.

It has been demonstrated that the new procedure, which possesses a dependence on a wide computational stencil that satisfies the criterion of being a *good neighborhood* for multidimensional limiting proposed in Ref. [52], is effective even on a grid that is composed of highly distorted triangles. The high-resolution strategy has been shown not to suffer from a catastrophic loss of accuracy, on a grid with poor connectivity, as revealed in Ref. [26] with many unstructured-grid limiting procedures. The limiter preserves the continuously differentiable property of the Osher flux-difference splitting scheme and would be well suited for the matrix-free version of GMRES currently being pursued as a convergence acceleration device for steady-state computations.

In would be desirable to extend the proposed high-resolution procedure to different cell types as required for a hybrid grid consisting of structured-quadrilateral cells in the near-field region and unstructured-triangular cells in the far-field region. Such an extension can be readily carried out in the case where the two regions are patched simply, with the interface common to a triangle and quadrilateral being shared on a one-to-one basis. A straightforward four-gradient generalization of the proposed reconstruction procedure would be required for the quadrilateral cells and it may work well since the grid distortions are not expected to be very severe for such cells. However, it would be more worthwhile to test the four-gradient generalization for a tetrahedra as required for three-dimensional unstructured-grid computations. The gradient at each of the four triangular interfaces would then be based on the Green–Gauss theorem applied to the union of two tetrahedra comprising three vertex and two cell-centered values.

APPENDIX

The gradient for a cell m using the new reconstruction procedure (Section 3) is obtained from the cell-centered gradients corresponding to the three neighbors a, b, and c as illustrated in Fig. 4 for a grid consisting of equilateral triangles. The gradients for cell a can be obtained by first computing the gradients at each interface and then combining the three interface gradients by an area-weighted procedure. The resulting cell-centered gradient involves the three vertex values of the cell apart from the cell center values of the three neighbors, yielding a hexagon-based procedure even for an arbitrary unstructured grid. The vertex values are computed using the pseudo-Laplacian approach as discussed in Section 3. The value of any of the primitive variables u at the vertex 1 can be written as (assuming equal weights here for equilateral triangles)

$$u_1 = \frac{1}{6}(u_m + u_a + u_b + u_d + u_e + u_f), \tag{A.1}$$

with similar expressions for u_3 and u_6 involving the corresponding cell-center values. The x and y components of the gradient for the face $1a3m$ are given by

$$(u_x)_{1a3m} = \frac{1}{2A_{1a3m}}[(u_m - u_a)y_{31} + (u_1 - u_3)y_{ma}] \tag{A.2}$$

$$(u_y)_{1a3m} = -\frac{1}{2A_{1a3m}}[(u_m - u_a)x_{31} + (u_1 - u_3)x_{ma}], \tag{A.3}$$

with analogous expressions for the faces $3a6l$ and $6a1d$. Area weighting of the three face gradients ensures cancellation at common interfaces and furnishes the gradient for cell a.

Equal areas yield weights of $1/3$ for the grid in Fig. 4; it can also be inferred that $y_{13} = 0$, $y_{ma} = 2y_{61}/3$, $x_{ma} = 0$, $y_{36} = -y_{61} = 3y_{al} = 3y_{ad}$, $x_{36} = x_{al} = x_{ad} = -x_{13}/2$, and $A_{136} = (A_{1a3m} + A_{3a6l} + A_{6a1d})/2$. Hence, the x and y components of the gradient for cell a can be written as

$$
\begin{aligned}
(u_x)_{1d6l3m} &= \frac{y_{61}}{2A_{136}}\left\{\frac{1}{2}(u_l - u_d) + \frac{1}{2}(u_3 - u_1)\right\} && \text{(A.4)}\\
&= \frac{y_{61}}{2A_{136}}\left\{\frac{7}{12}(u_l - u_d) + \frac{1}{12}(u_c + u_j + u_k) - \frac{1}{12}(u_b + u_e + u_f)\right\} && \text{(A.5)}\\
(u_y)_{1d6l3m} &= \frac{x_{13}}{2A_{136}}\left\{\frac{2}{3}\left[\frac{(u_m - u_6)}{4/3}\right] + \frac{1}{3}\left[\frac{(u_1 + u_3)/2 - (u_d + u_l)/2}{2/3}\right]\right\} && \text{(A.6)}\\
&= \frac{x_{13}}{2A_{136}}\left\{\frac{7}{12}\left[u_m - \frac{(u_d + u_l)}{2}\right] + \frac{1}{12}\left[\frac{1}{2}(u_b + u_c + u_e + u_f + u_j + u_k)\right.\right.\\
&\qquad \left.\left. - (u_A + u_D + u_L)\right]\right\}. && \text{(A.7)}
\end{aligned}
$$

Equations (A.4) and (A.6) reveal that the gradient is centered at the centroid of cell a.

It must be mentioned that for the x and y components of the gradient, the contributions from cell a vanish only for a grid consisting of equilateral triangles. It should also be noted that Eqs. (A.4) and (A.6) are similar in form to those presented in Ref. [53] for vertex-based finite-difference schemes, which have been derived based on phase-error considerations rather than from the Green–Gauss theorem and are limited to regular triangular grids.

Similar expressions can be written for cells b and c. The limited gradient for cell m is obtained using the weighted average of the gradients in cells a, b, and c in which the weights are computed from the limiter function described in Section 4. To ensure cancellation at common interfaces the unlimited gradients can be obtained using the area-weighted averages, which results in weights of $1/3$ each. The expressions for the x and y components of the gradient are given as

$$
\begin{aligned}
(u_x)_m &= \frac{1}{3}[(u_x)_a + (u_x)_b + (u_x)_c] && \text{(A.8)}\\
&= \frac{y_{12}}{2A_{132}}\left\{\frac{1}{18}\left[(u_c - u_b) + \frac{1}{2}\left(\frac{u_k - u_e}{2}\right)\right] + \frac{1}{18}\left[\left(\frac{u_I - u_G}{3}\right) + \frac{1}{2}\left(\frac{u_k - u_e}{2}\right)\right]\right.\\
&\quad + \frac{1}{36}\left[\left(\frac{u_I - u_G}{3}\right) + \frac{1}{3}(u_l - u_d)\right] + \frac{1}{12}\left[\frac{1}{3}(u_i - u_g) + \frac{1}{3}(u_l - u_d)\right]\\
&\quad + \frac{1}{4}\left[\frac{1}{3}\left(\frac{u_C - u_B}{3}\right) + \frac{1}{3}(u_l - u_d)\right] + \frac{2}{9}\left[\frac{1}{4}\left(\frac{u_J - u_F}{2}\right) + \frac{1}{3}(u_l - u_d)\right]\\
&\quad \left. + \frac{1}{18}\left(\frac{u_j - u_f}{2}\right)\right\} && \text{(A.9)}\\
&= \frac{y_{12}}{2A_{132}}\left\{\frac{1}{36}\left[2u_c + u_i + 8u_j + u_k + 7u_l + u_C + u_I + u_J\right]\right.\\
&\quad \left. - \frac{1}{36}[2u_b + 7u_d + u_e + 8u_f + u_g + u_B + u_F + u_G]\right\} && \text{(A.10)}
\end{aligned}
$$

$$(u_y)_m = \frac{1}{3}[(u_y)_a + (u_y)_b + (u_y)_c] \tag{A.11}$$

$$\begin{aligned} &= \frac{x_{13}}{2A_{132}}\left\{\frac{1}{18}\left[\left(\frac{u_b + u_c}{2}\right) - u_a\right] + \frac{1}{36}\left[\left(\frac{u_G + u_C}{2}\right) - \left(\frac{u_e + u_k}{2}\right)\right]\right. \\ &\quad + \frac{1}{2}\left[\frac{(u_g + u_c)/2 - (u_d + u_l)/2}{2}\right] + \frac{1}{6}\left[\left(\frac{u_g + u_c}{2}\right) - \left(\frac{u_f + u_j}{2}\right)\right] \\ &\quad + \frac{1}{12}\left[\frac{u_h - (u_f + u_j)/2}{2}\right] + \frac{1}{12}\left[\frac{(u_F + u_J)/2 - (u_D + u_L)/2}{2}\right] \\ &\quad \left. + \frac{1}{18}\left[\frac{(u_B + u_C)/2 - u_A}{2}\right]\right\} \end{aligned} \tag{A.12}$$

$$\begin{aligned} &= \frac{x_{13}}{2A_{132}}\left\{\left[\frac{1}{18}\left(\frac{u_b + u_c}{2}\right) + \frac{5}{12}\left(\frac{u_g + u_i}{2}\right) + \frac{1}{36}u_h + \frac{1}{36}\left(\frac{u_B + u_C}{2}\right)\right.\right. \\ &\quad \left. + \frac{1}{36}\left(\frac{u_F + u_J}{2}\right) + \frac{1}{36}\left(\frac{u_G + u_I}{2}\right)\right] - \left[\frac{1}{18}u_a + \frac{1}{4}\left(\frac{u_d + u_l}{2}\right)\right. \\ &\quad \left.\left. + \frac{1}{36}\left(\frac{u_e + u_k}{2}\right) + \frac{1}{6}\left(\frac{u_f + u_j}{2}\right) + \frac{1}{36}u_A + \frac{1}{18}\left(\frac{u_D + u_L}{2}\right)\right]\right\}, \end{aligned} \tag{A.13}$$

where A_{132} is the area of computational cell $\triangle_{123}$. It may be noted that in this particular case, the x and y components of the gradients, respectively, possess a dependence on stencils with 16 and 21 points.

For Frink's reconstruction, the expressions for the gradients in cell m can be written as

$$(u_x)_m = \frac{1}{2A_{132}}[u_1 y_{23} + u_2 y_{31} + u_3 y_{12}] = \frac{y_{12}}{2A_{132}}[u_3 - u_1] \tag{A.14}$$

$$(u_y)_m = -\frac{1}{2A_{132}}[u_1 x_{23} + u_2 x_{31} + u_3 x_{12}] = \frac{x_{13}}{2A_{132}}\left[u_2 - \frac{(u_1 + u_3)}{2}\right]. \tag{A.15}$$

This indicates that the x and y components of the gradient are centered at $((x_1 + x_3)/2, y_1)$ and $((x_1 + x_3)/2, (y_1 + y_2)/2)$, respectively. Substituting for the cell-vertex values in terms of the cell-center values we can write the above equations as

$$(u_x)_m = \frac{y_{12}}{2A_{132}}\left\{\frac{1}{6}(u_c - u_b) + \frac{1}{6}(u_j + u_k + u_l) - \frac{1}{6}(u_d + u_e + u_f)\right\} \tag{A.16}$$

$$\begin{aligned} (u_y)_m &= \frac{x_{13}}{2A_{132}}\left\{\frac{1}{6}\left[\left(\frac{u_b + u_c}{2}\right) - u_a\right]\right. \\ &\quad \left. - \frac{1}{6}\left[(u_g + u_h + u_i) - \frac{1}{2}(u_j + u_k + u_l + u_d + u_e + u_f)\right]\right\}. \end{aligned} \tag{A.17}$$

This clearly shows that Frink's construction leads to 8- and 12-point stencils that respectively determine the x and y components of the gradient.

Similar expressions for the x and y components of the gradient can be written using Barth and Jespersen's 3-point stencil, which involves only the cell-center values of the nearest neighbors:

$$(u_x)_m = \frac{1}{2A_{132}}[u_a y_{bc} + u_b y_{ca} + u_c y_{ab}] = \frac{y_{12}}{2A_{132}}[u_c - u_b] \tag{A.18}$$

$$(u_y)_m = -\frac{1}{2A_{132}}[u_a x_{bc} + u_b x_{ca} + u_c x_{ab}] = \frac{x_{13}}{2A_{132}}\left[\left(\frac{u_b + u_c}{2}\right) - u_a\right]. \quad \text{(A.19)}$$

The gradients for the cell m using Barth and Jespersen's 12-point stencil can be obtained by area-weighted averaging of the gradients at its three vertices 1, 2, and 3. The gradients at a vertex are computed by applying the Green–Gauss theorem to the cell-centered values that are common to a vertex. The average of the vertex gradients then yields the gradients at the centroid of a cell. The two components of the gradient obtained using this procedure are

$$\begin{aligned}
(u_x)_m &= \frac{y_{12}}{2A_{132}}\left\{\frac{1}{6}[(u_c - u_b) + (u_i - u_g) + (u_j - u_f) + (u_k - u_e)]\right\} && \text{(A.20)}\\
&= \frac{y_{12}}{2A_{132}}\left\{\frac{1}{6}(u_c + u_i + u_j + u_k) - \frac{1}{6}(u_b + u_e + u_f + u_g)\right\} && \text{(A.21)}\\
(u_y)_m &= \frac{x_{13}}{2A_{132}}\left\{\frac{1}{6}\left[(u_b - u_d) + \left(\frac{(u_m - u_a) + (u_f - u_e)}{2}\right)\right]\right.\\
&\quad + \frac{1}{6}\left[(u_h - u_m) + \left(\frac{(u_i - u_c) + (u_g - u_b)}{2}\right)\right]\\
&\quad \left. + \frac{1}{6}\left[(u_c - u_i) + \left(\frac{(u_j - u_k) + (u_m - u_a)}{2}\right)\right]\right\} && \text{(A.22)}\\
&= \frac{x_{13}}{2A_{132}}\left\{\frac{1}{12}[u_b + u_c + u_f + u_g + 2u_h + u_i + u_j]\right.\\
&\quad \left. - \frac{1}{12}[2u_a + 2u_d + u_e + u_k + 2u_l]\right\}. && \text{(A.23)}
\end{aligned}$$

This indicates that the x and y components of the gradient depend on stencils with 8 and 12 points, respectively. A comparison with Frink's construction reveals that the points involved are the same for y, but with a different formula altogether, but not for the x gradients.

ACKNOWLEDGEMENTS

The first author acknowledges the financial support provided by CSIR (India) during a significant duration of this research work. The second author thanks Prof. Rolf Jeltsch, Seminar für Angewandte Mathematik, ETH, Zürich for extending generous hospitality during a recent sabbatical at the Swiss Federal Institute of Technology where some concluding portions of this manuscript were written. Also, thanks are due to Dr. V. Venkatakrishnan, formerly at ICASE, for providing the subroutine for the perturbation of a structured-triangulated grid. The authors acknowledge the constructive criticism of the five anonymous reviewers whose careful reading led to substantial improvement of the manuscript. The work of the second author was partly supported by the Swiss National Science Foundation Grant Nr. 21-52251.97.

REFERENCES

1. V. Venkatakrishnan, Perspective on unstructured grid flow solvers, *AIAA J.* **34**(3), 533 (1996).
2. D. J. Mavriplis, Unstructured grid techniques, *Annu. Rev. Fluid. Mech.* **29**, 473 (1997).
3. T. J. Barth, Aspects of unstructured grids and finite-volume solvers for the Euler and Navier–Stokes equations, *AGARD Rep.* **787** (1992).
4. L. Fezoui and B. Stoufflet, A class of implicit upwind schemes for Euler simulations with unstructured meshes, *J. Comput. Phys.* **84**, 174 (1989).

5. V. Venkatakrishnan and T. J. Barth, Application of direct solvers to unstructured meshes for the Euler and Navier–Stokes equations using upwind schemes, *AIAA Pap. 89-0364* (1989).
6. J. T. Batina, Three-dimensional flux-split Euler schemes involving unstructured dynamic meshes, *AIAA Pap. 90-1649* (1990).
7. D. C. Slack, D. L. Whitaker, and R. W. Walters, Time integration algorithms for the two-dimensional Euler equations on unstructured meshes, *AIAA J.* **32**(6) (1994).
8. B. van Leer, Towards the ultimate conservative difference scheme V, A second order sequel to Godunov's method, *J. Comput. Phys.* **32**, 101 (1979).
9. T. J. Barth and D. C. Jespersen, The design and application of upwind schemes on unstructured meshes, *AIAA Pap. 89-0366* (1989).
10. J. Cabello, K. Morgan, and R. Lohner, A comparison of higher order schemes used in a finite volume solver for unstructured grids, *AIAA Pap. 94-2293* (1994).
11. G. D. van Albada, B. van Leer, and W. W. Roberts, A comparative study of computational methods in cosmic gas dynamics, *Astron. Astrophys.* **108**, 76 (1982).
12. W. K. Anderson, J. L. Thomas, and B. van Leer, A comparison of finite volume flux vector splittings for the Euler equations, *AIAA J.* **24**, 1453 (1986).
13. V. Venkatakrishnan, Convergence to steady state solutions of the Euler equations on unstructured grids with limiters, *J. Comput. Phys.* **118**, 120 (1995).
14. M. Aftosmis, D. Gaitonde, and T. S. Tavares, Behaviour of linear reconstruction techniques on unstructured meshes, *AIAA J.* **33**(11), 2038 (1995).
15. A. Harten, High resolution schemes for hyperbolic conservation laws, *J. Comput. Phys.* **49**, 357 (1983).
16. J. R. Amaladas and H. Kamath, Accuracy assessment of upwind algorithms for steady-state computations, *Comput. Fluids* **27**(8), 941 (1998).
17. N. T. Frink, Upwind scheme for solving the Euler equations on unstructured tetrahedral meshes, *AIAA J.* **30**(1), 70 (1992).
18. N. T. Frink, Recent progress towards a three-dimensional unstructured Navier–Stokes flow solver, *AIAA Pap. 94-0061* (1994).
19. D. G. Holmes and S. D. Connell, Solution of the 2D Navier–Stokes equations on unstructured adaptive grids, *AIAA Pap. 89-1932 in Proc. AIAA 9th CFD Conference* (1989).
20. N. T. Frink and S. Z. Pirzadeh, Tetrahedral finite-volume solutions to the Navier–Stokes equations on complex configurations, in *Proc. 10th International Conference on Finite Elements in Fluids, Tucson, AZ* (1998).
21. D. Pan and J. C. Cheng, Upwind finite-volume Navier–Stokes computations on unstructured triangular meshes, *AIAA J.* **31**(9), 1618 (1993).
22. B. van Leer, Towards the ultimate conservative difference scheme III, Upstream-centered finite-difference schemes for ideal compressible flow, *J. Comput. Phys.* **23**, 263 (1977).
23. A. Hosangadi, R. A. Lee, B. J. York, N. Sinha, and S. M. Dash, Upwind unstructured scheme for three-dimensional combusting flows, *J. Propul. Power* **12**(3), 494 (1996).
24. J. V. Rosendale, Floating shock fitting via Lagrangian adaptive meshes, *ICASE 94-89* (1989).
25. P. Batten, C. Lambert, and D. M. Causon, Positively conservative high-resolution convection schemes for unstructured elements, *Int. J. Numer. Meth. Eng.* **39**, 1821 (1996).
26. M. E. Hubbard, Multidimensional slope limiters for MUSCL-type finite volume schemes on unstructured grids, *J. Comput. Phys.* **155**, 54 (1999).
27. L. J. Durlofsky, B. Engquist, and S. Osher, Triangle based adaptive stencils for the solution of hyperbolic conservation laws, *J. Comput. Phys.* **98**, 64 (1992).
28. K. G. Powell and B. van Leer, Tailoring explicit time-marching schemes to improve convergence characteristics, *von Karman Institute Lecture Series* **90-03** (1992).
29. H. Viviand, Numerical solutions of two-dimensional reference test cases, *AGARD-AR-211*, 1985. Also see T. H. Pulliam and J. T. Barton, Euler computations of AGARD working group 07, Airfoil test cases, *AIAA Pap. 85-0018* (1985).

30. A. Dervieux, B. van Leer, J. Periaux, and A. Rizzi, Numerical simulation of compressible Euler flows, *Notes Numer. Fluid Dyn.* **26**. Vieweg, Braunschweig, (1989). Also see *Proceedings of the GAMM-Workshop on Numerical Simulation of Compressible Navier–Stokes Flows, INRIA, Sophia-Antipolis; Notes Numer. Fluid Mech.* **18** (1986).
31. W. K. Anderson, A grid generation and flow solution method for the Euler equations on unstructured grids, *J. Comput. Phys.* **110**, 23 (1994).
32. J. L. Thomas and M. D. Salas, Far-field boundary conditions for transonic lifting solutions to the Euler equations, *AIAA J.* **24**(7), 1074 (1986).
33. R. C. Swanson, R. Radespiel, and E. Turkel, On some numerical dissipation schemes, *J. Comput. Phys.* **147**, 518 (1998).
34. D. K. Clarke, M. D. Salas, and H. A. Hassan, Euler computations for multielement airfoils using Cartesian grids, *AIAA J.* **24**(3), 353 (1986).
35. K. Morinishi, A finite difference solution of the Euler equations on non-body-fitted Cartesian grids, *Comput. Fluids* **21**(3), 331 (1992).
36. C. J. Hwang and S. J. Wu, Global and local remeshing algorithms for compressible flows, *J. Comput. Phys.* **102**, 98 (1992).
37. W. J. Coirier and K. G. Powell, An accuracy assessment of Cartesian-mesh approaches for the Euler equations, *J. Comput. Phys.* **117**, 121 (1995).
38. Z. N. Wu, Convergence study of an implicit multidomain approximation for the compressible Euler equations, *Comput. Fluids* **25**(2), 181 (1996).
39. A. Lerat and Z. N. Wu, Stable conservative multidomain treatments for implicit Euler solvers, *J. Comput. Phys.* **123**, 45 (1996).
40. M. O. Bristeau, R. Glowinski, J. Periaux, and H. Viviand, Numerical simulation of compressible Navier–Stokes flows, *Notes Numer. Fluid Dyn.* **18**, Vieweg, Braunschweig (1987).
41. A. Haselbacher, J. J. McGuirk, and G. J. Page, Finite volume discretization aspects for viscous flows on mixed unstructured grids, *AIAA J.* **37**(2), 177 (1999).
42. D. J. Mavriplis and A. Jameson, Multigrid solution of Navier–Stokes equations on triangular meshes, *AIAA J.* **28**(8), 1415 (1990).
43. M. Hafez, Finite element and finite volume solutions of full potential, Euler and Navier–Stokes equations for compressible and incompressible flows, *Int. J. Numer. Meth. Fluids* **20**, 713 (1995).
44. F. Bassi and S. Rebay, A high-order accurate discontinuous finite element method for the numerical solution of the compressible Navier–Stokes equations, *J. Comput. Phys.* **131**, 267 (1997).
45. P. A. Forsyth and H. Jiang, Nonlinear iteration methods for high speed laminar compressible Navier–Stokes equations, *Comput. Fluids* **26**(3), 249 (1997).
46. A. Meister, Comparison of different Krylov subspace methods embedded in an implicit finite volume scheme for the computation of viscous and inviscid flow fields on unstructured grids, *J. Comput. Phys.* **140**, 311 (1998).
47. S. Pirzadeh, Three-dimensional unstructured viscous grids by the advancing-layers method, *AIAA J.* **34**(1), 43 (1996).
48. V. Venkatakrishnan, Viscous computations using a direct solver, *Comput. Fluids* **18**(2), 191 (1990).
49. R. Radespiel and R. C. Swanson, An investigation of cell centered and cell vertex multigrid schemes for the Navier–Stokes equations, *AIAA Pap. 89-0453*, 1989.
50. P. I. Crumpton, J. A. Mackenzie, and K. W. Morton, Cell vertex algorithms for the compressible Navier–Stokes equations, *J. Comput. Phys.* **109**, 1 (1993).
51. D. De Zeeuw and K. G. Powell, An adaptively refined Cartesian mesh solver for the Euler equations, *J. Comput. Phys.* **104**, 56 (1993).
52. B. Swartz, Good neighborhoods for multidimensional van Leer limiting, *J. Comput. Phys.* **154**, 237 (1999).
53. D. W. Zingg and H. Lomax, Finite-difference schemes on regular triangular grids, *J. Comput. Phys.* **108**, 306 (1993).